ACSNANO

www.acsnano.org

ARTICLE

Down-Regulating Scar Formation by Microneedles Directly *via* a Mechanical Communication Pathway

Qing Zhang, Lin Shi, Hong He, Xingmou Liu, Yong Huang, Dan Xu, Mengyun Yao, Ning Zhang, Yicheng Guo, Yifei Lu, Haisheng Li, Junyi Zhou, Jianglin Tan,* Malcolm Xing,* and Gaoxing Luo*

Cite This: *ACS Nano* 2022, 16, 10163–10178

Read Online

ACCESS | Metrics & More | Article Recommendations | Supporting Information

ABSTRACT: **Excessive extracellular matrix deposition drives fibroblasts into a state of high mechanical stress, exacerbating pathological fibrosis and hypertrophic scar formation, leading to tissue dysfunction. This study reports a minimally invasive and convenient approach to obtaining scarless tissue using a silk fibroin microneedle patch (SF MNs). We found that by tuning the MN size and density only, the biocompatible MNs significantly decreased the scar elevation index in the rabbit ear hypertrophic scar model and increased ultimate tensile strength close to regular skin. To advance our understanding of this recent approach, we built a fibroblast-populated collagen lattice system and finite element model to study MN-mediated cellular behavior of fibroblasts. We found that the MNs reduced the fibroblasts generated contraction and mechanical stress, as indicated by decreased expression of the mechanical sensitive gene ANKRD1. Specifically, SF MNs attenuated the integrin-FAK signaling and consequently down-regulated the expression of TGF-β1, α-SMA, collagen I, and fibronectin. It resulted in a low-stress microenvironment that helps to reduce scar formation significantly. Microneedles' physical intervention *via* the mechanotherapeutic strategy is promising for scar-free wound healing.**

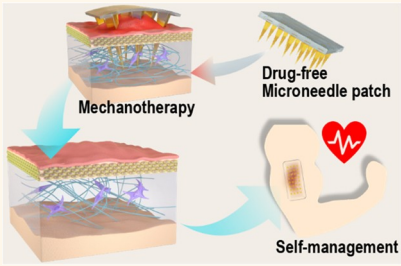

KEYWORDS: *microneedle, hypertrophic scar, mechanical communication, integrin-FAK signaling, mechanotherapy*

Hypertrophic scars (HSs), a pathological scar affecting 70% of post trauma, present an extraordinarily stiff bulge, tensile strength reduction, and pigmentation disorder.[1−5] An HS induces pruritus, chronic pain, loss of limb mobility, and anxiety and depression in patients. HSs are still a significant challenge in wound management after injury.[1,5−7]

Accompanied by the overgrowth of fibrosis, an HS usually happens in the locations of high tension and stiffness, such as the joints, chest, upper back, and shoulder.[8,9] Given this, mechanical force and its derived stress field have been identified as crucial factors in pathological fibrosis development.[8,10−14] In response to mechanical stress, fibroblasts display an activated phenotype, the myofibroblasts, showing distinctive contraction. Meanwhile, the transforming growth factor (TGF-β1), α-smooth muscle actin (α-SMA), and connective tissue growth factor (CTGF) are all significantly up-regulated, and the type I collagen and fibronectin secreted by myofibroblasts are overexpressed as well. The excessive and disordered deposition of the extracellular matrix (ECM, mainly collagen and fibronectin) will result in pathological changes of fibrosis and formation of hypertrophic scars.[14−19] As a positive feedback, stiff tissue induces the fibroblasts to generate stronger forces, which promotes pathologic fibrosis.[3,11,20−23] Therefore, the mechanical interaction has been an efficient approach in HS therapy by decreasing mechanical stress to inhibit fibroblasts' activation and down-regulate profibrotic cytokine expression.[21,22,24]

Although a broad range of therapeutic strategies such as surgical intervention, compression garments, laser therapy, and massage have been used to reduce tissue tension in HSs, they are still far from perfect.[15] For instance, z-plasty can disperse mechanical force effectively in incisions after cicatrectomy, yet the incision induces a secondary injury and potential risk of scarring.[25] Compression garments decrease vascularization and remodel collagen formation to obtain an improved aesthetic appearance only within a long protocol of treatment period.[1] Laser therapy destroys the disorganized collagen *via* thermal effects and changes the mechanical environment and ultrastructure of scar tissue. Still, patients may suffer from adverse effects such as bleeding, erythema, purpura, and possible

Received: December 11, 2021
Accepted: May 19, 2022
Published: May 26, 2022

https://doi.org/10.1021/acsnano.1c11016
ACS Nano 2022, 16, 10163−10178

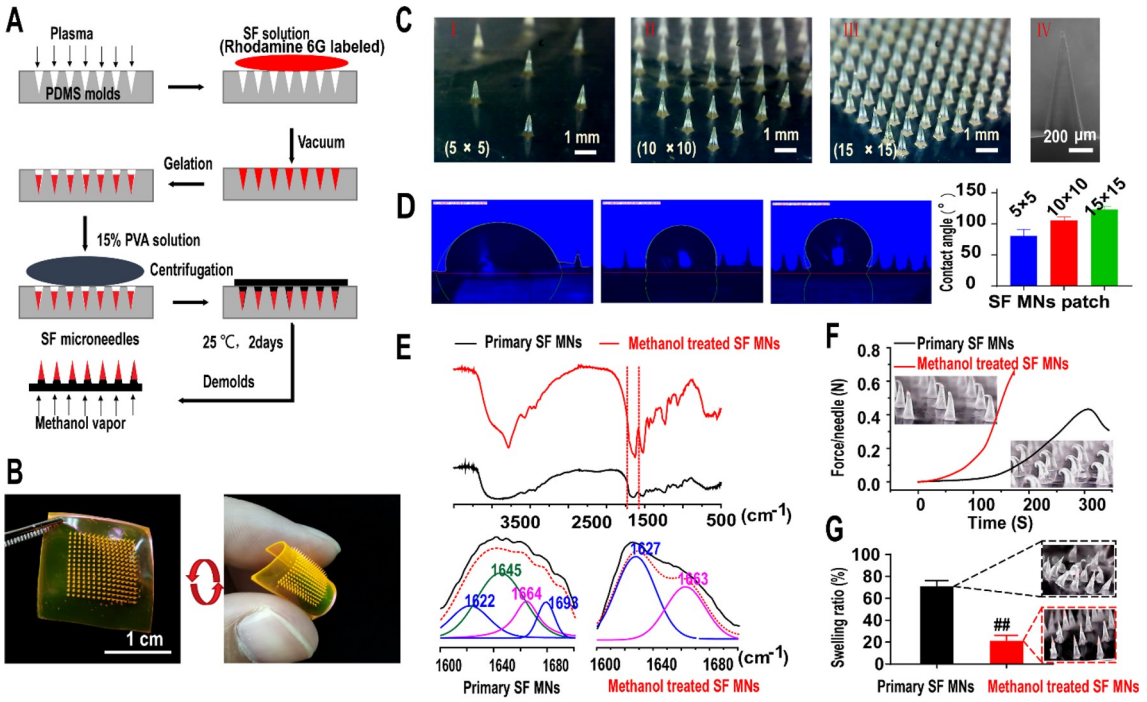

Figure 1. Fabrication and characterization of silk fibroin microneedle patches. (A) Manufacturing process of silk fibroin microneedle patches (SF MNs). (B) Array of 15 × 15 silk fibroin microneedle patch with a soft backing layer, labeled with rhodamine 6G. Scale bar, 1 cm. (C) Digital photograph of three different arrays of SF MN patches (I, II, III) with a height of 917 ± 19 μm (IV). Scale bars, 1 mm (left) and 200 μm (right). (D) Surface energy indicated by measuring the contact angles formed with a liquid collagen droplet. A significantly increased contact angle occurred with the increase in the density of the microneedles array (5 × 5: 80.38 ± 9.98°, 10 × 10: 104.99 ± 5.64°, and 15 × 15: 122.89 ± 5.28°). (E) FTIR spectra and secondary structure analysis of the natural and methanol-treated samples, respectively. (F) Compression test of SF MNs. The methanol-treated SF microneedle could withstand compressive forces of more than 0.6 N per needle. (G) Swelling ratio of SF MNs after being inserted into porcine skin for 24 h.

ulceration.[26−28] Moreover, these approaches are highly dependent on the skills of the clinician. So far, in HS mechanotherapy, a less invasive, convenient, but effective approach is still illusive.

Recently, researchers have performed a lot of exciting work using microneedles (MNs) as powerful tools with inherent painlessness and minimal invasion to implement subcutaneous substance exchange (either drug delivery or sampling).[29−35] However, the therapeutic effects of MNs themselves have usually been neglected. Herein, we hypothesize that MNs can tune the biomechanics and ultrastructure of tissue by penetrating through the epidermis into the dermis and creating arrays of microholes, thereby creating a scar-free environment in a minimally invasive way.

To test our hypothesis, we studied the efficacy and mechanism of polymeric microneedles to remodel hypertrophic scars and explored the mechanism of underlying mechanotransduction. We used silk fibroin, a natural material with tunable stiffness and strength,[36,37] for the fabrication of MN patches. Scar elevation index, tissue stiffness, ultimate tensile strength, and ECM ultrastructure were investigated. A fibroblast-populated collagen lattice system (FPCL) and a finite element model were built to demonstrate the changes in fibroblast-generated contraction and mechanical environment of the ECM under the MN intervention. To clarify the scar-free microenvironment, we further identified the mechanism of fibroblast response to the MN intervention by singling out the molecular signal transduction pathway *via* transcriptome sequencing and verifying the expression of essential proteins (including ANKRD1, FAK/p-FAK, RhoA, F-actin, vinculin, TGF-β1, α-SMA, collagen I, fibronectin) *in vitro* and *in vivo*.

RESULTS AND DISCUSSION

Fabrication and Characterization of a Microneedle Patch of Silk Fibroin. Figure 1A and Figure S1 illustrate a two-step template replication process to fabricate a silk fibroin microneedle (SF MN) patch. A silk fibroin solution (10 wt %) was cast over a plasma-treated polydimethylsiloxane (PDMS) microneedle template under vacuum (0.07−0.1 MPa), and the hydrogel was formed due to noncovalent interactions of hydrogen bonding, hydrophobic interaction, and chain winding in silk fibroin molecules.[38] After sol−gel transition and then a 60 °C oven overnight, the primary SF MNs reproduced the master mold successfully. Rhodamine 6G was incorporated into the fabrication for visualization. As shown in Figure 1b of a 15 × 15 patch with a polyvinyl acetate (PVA) backing layer, the microneedle was pyramid in shape with a side length of 300 μm at the base. Generally, a hypertrophic scar is nonuniform in thickness, usually ranging from 0.5 to 2 mm in the rabbit ear HS model.[39,40] The needles with a length of 500, 1000, and 1500 μm were fabricated to evaluate the length effects of MNs (Figure S2A). As shown in Figure S2B, the 500 μm MN was too short to achieve an efficient penetration. With the increasing length of the needle, the penetration improved. However, in most cases (6 out of 12 cases), there were adverse effects such as bleeding and an inflammatory response for the group of 1500 μm MNs. After 2 weeks' treatment, the therapeutic efficacy was evaluated in the thickness of HS tissues and scar elevation index (SEI). Compared to the

https://doi.org/10.1021/acsnano.1c11016
ACS Nano 2022, 16, 10163−10178

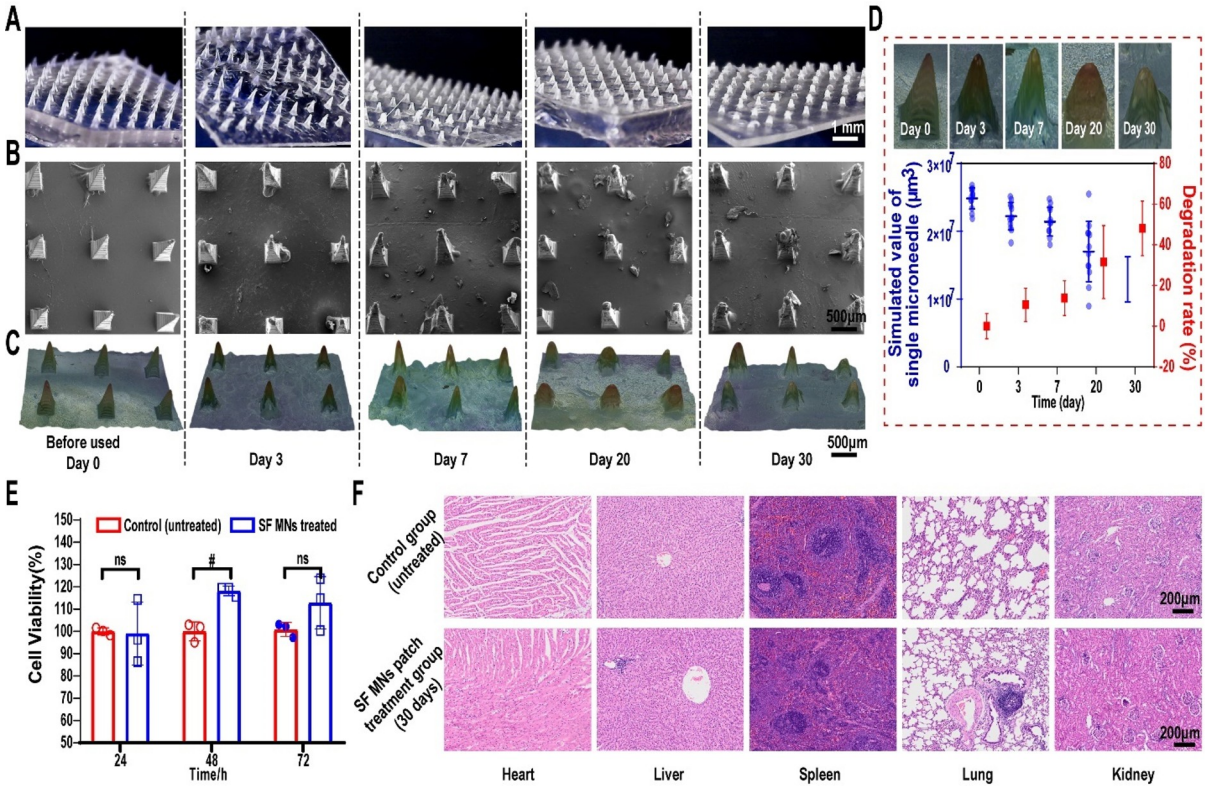

Figure 2. ***In vivo*** **degradation and biocompatibility of SF MNs. The morphology of the SF MN patch before use (0 day) and after insertion in the rabbit ear scar for 3, 7, 20, and 30 days was characterized by (A) optical microscope (scale bar, 1 mm) and (B) scanning electron microscope (scale bar, 500 μm). (C) 3D scanning and reconstruction using a Leica DVM6 digital microscope with LAS X software from Leica microsystems (Leica, Germany) (scale bar, 500 μm). (D) Degradation rate of a single microneedle according to the 3D images from (C). (E) Cytotoxicity of SF MNs measured by the CCK-8 assay. ns and $^{\#}p < 0.05$ stand for non- and significant difference in cell viability of fibroblasts between the control and SF MN treated group, respectively. (F) Tissue sections of the heart, liver, lung, spleen, and kidney of the rabbit treated with or without an SF MN patch for 30 days. Scale bar, 200 μm.**

limited therapeutic efficacy of 500 μm MNs (thickness: 1709.41 ± 570.38 μm, SEI: 4.21 ± 0.76), significant improvements were achieved in the group of 1000 μm (thickness: 1178.25 ± 79.84 μm, SEI: 2.67 ± 0.39), which was also slightly better than the group of 1500 μm (thickness: 1654.15 ± 293.44 μm, SEI: 3.79 ± 0.80) (Figure S2C). Thus, the 1 mm height was an appropriate size in this study.

To tune the mechanical interaction between the needles and the tissue, three needle pitches of 2300, 1070, and 690 μm were considered in the SF MNs patches as arrays of 5 × 5, 10 × 10, and 15 × 15 over a 1.0 cm^2 area, respectively (Figure 1C and Figure S1). Contact angle changes on liquid collagen droplets showed that the array densities of MNs can lead to a change of surface energy. The hydrophobicity increased with the density of microneedles, as indicated by a significantly large contact angle of 122.89 ± 5.28° on a 15 × 15 MN patch, compared with 80.38 ± 9.98° for 5 × 5 and 104.99 ± 5.64° for 10 × 10 (Figure 1D). From a mechanical perspective, increasing the needle density induces more penetration into the scar tissue, which can enhance resistance to the deformation caused by cell directional migration and in-growth. From a physical perspective, a larger needle density induces an elevated contact angle or hydrophobicity of the patch, which, on the other hand, may also restrict cell migration and proliferation,[41] which leads to potentially decreasing fibroblast-generated contractile stress in scar tissue.

In order to achieve efficient penetration into the scar tissue and physical interaction, the primary silk microneedles were further modified by methanol vapor annealing to promote the secondary structure of SF molecules transformed from the random coil to β-sheet conformation.[42] Increasing the β-sheet content yields silk materials with lower degradation and solubility, but higher crystallinity and breaking strength.[36,37,43,44] Postprocessed by methanol vapor annealing overnight, the SF MNs reached a much higher content of β-sheet secondary structure than primary SF, which was confirmed using the Fourier-transform infrared spectroscopy (FTIR) method. The peak devolution of the amide I region was performed using a secondary derivative method in *Peakfit* software. The raw spectra (1600−1700 cm^{-1}) were assigned to a variety of secondary structures, respectively: 1620−1630 cm^{-1}/1690−1700 cm^{-1} (β-sheet), 1635−1664 cm^{-1} (random coil/helix), and 1666−1690 cm^{-1} (β-turn) (Figure 1E).[45,46] Compared to the low amounts of the β-sheet structure of primary SF material (~25.6%), methanol treatment induced a much higher content of β-sheet crystalline structure[36,47] of the methanol-treated SF MNs (~60%) (Table S1). Also, methanol vapor annealing improved the mechanical strengths of the SF MN patch. Each treated SF MN (with a bottom x−y section area of 0.09 mm^2) can withstand more than 0.65 N of compressive force and a yield stress of up to 7.2 MPa, compared to 0.43 N of a primary SF MN (yield stress: 4.7 MPa) (Figure 1F). It took about 0.5 N for a single needle to successfully penetrate the HS tissue.[29] Methanol vapor annealing induced a low solubility of SF MNs, consistent with the decreasing swelling ratio of ~21.8% in 24 h compared

https://doi.org/10.1021/acsnano.1c11016
ACS Nano 2022, 16, 10163−10178

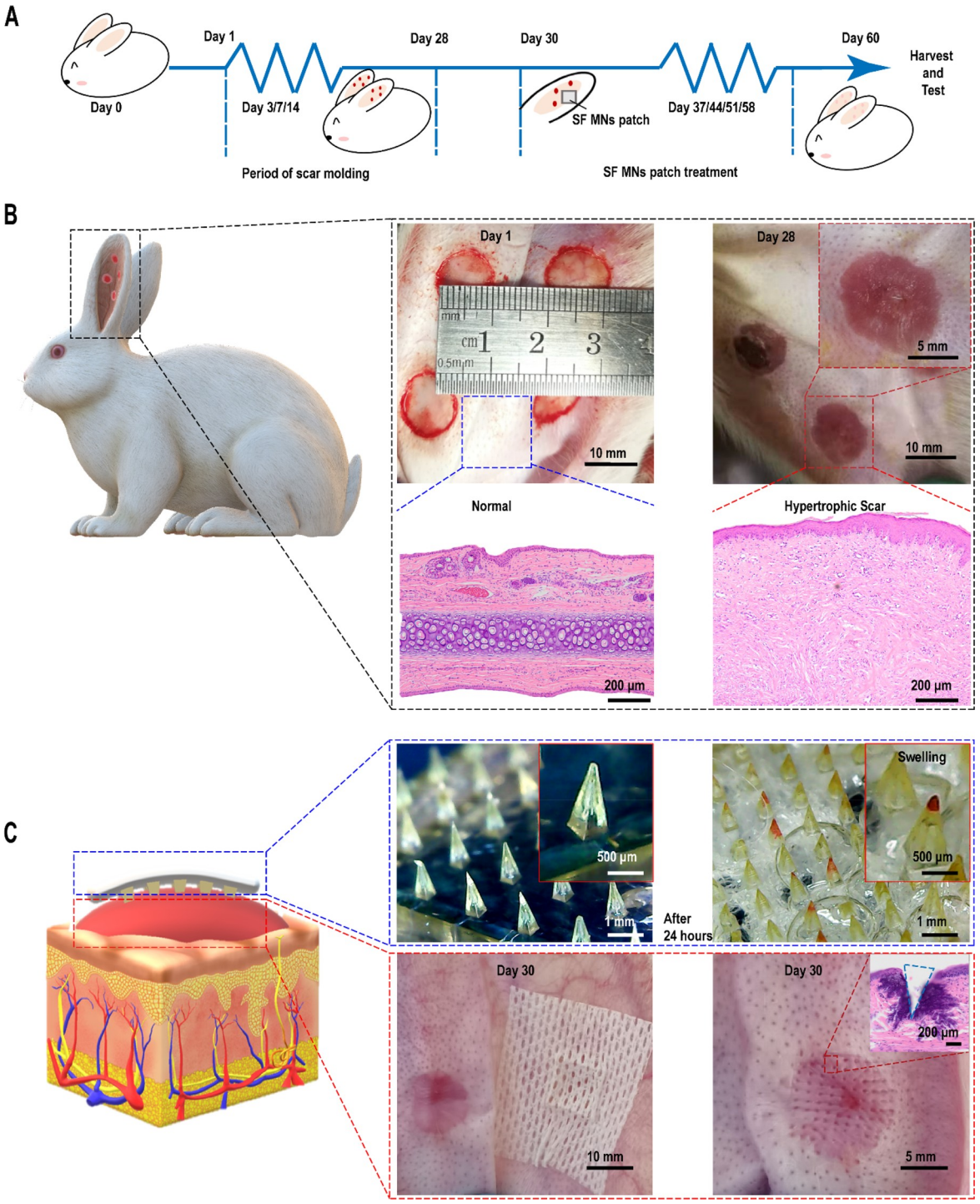

Figure 3. Illustration of the construction of animal models and SF MN patch treatment. (A) Time nodes of different stages of the whole experimental process. (B) On day 28, four rabbit ear scar models were established successfully on the ventral side of each rabbit ear, as evidenced by the apparent excess and disordered collagen deposition in the pathological scar tissue compared to the normal tissue. Scale bars, 10 mm, 5 mm, and 200 μm. (C) On day 30, SF MN patches were employed to treat the hypertrophic scars. Successful penetration was verified by tissue sectioning and H&E staining. Scale bars, 10 mm, 5 mm, 1 mm, 500 μm, and 200 μm.

to 74.8% of primary SF MNs (Figure 1G). It also slowed the degradation of the MNs. As for the degradation *in vivo*, the 2D images of SF MN patches before use (day 0) and after 3-, 7-, 20-, and 30-day penetration were obtained using an optical microscope (Figure 2A) and scanning electron microscope (SEM) (Figure 2B). We found that MNs displayed intact structures before and after penetration. With the prolonging of the retention time, its taper-like sharp shape structure erosion gradually happened but in a controlled way. To quantify the degradation, 3D scanning and reconstructed implanted patches were then statistically analyzed for the volume of a single remnant microneedle (Figure 2C). It showed that the average volume of a single microneedle declined from $(2.48 \pm 0.15) \times 10^{-2}$ mm^3 to $(1.29 \pm 0.31) \times 10^{-2}$ mm^3. A long duration of 30 days can guarantee an adequate physical intervention for therapy. The degradation rate did not exceed 50% (~48%)

https://doi.org/10.1021/acsnano.1c11016
ACS Nano 2022, 16, 10163−10178

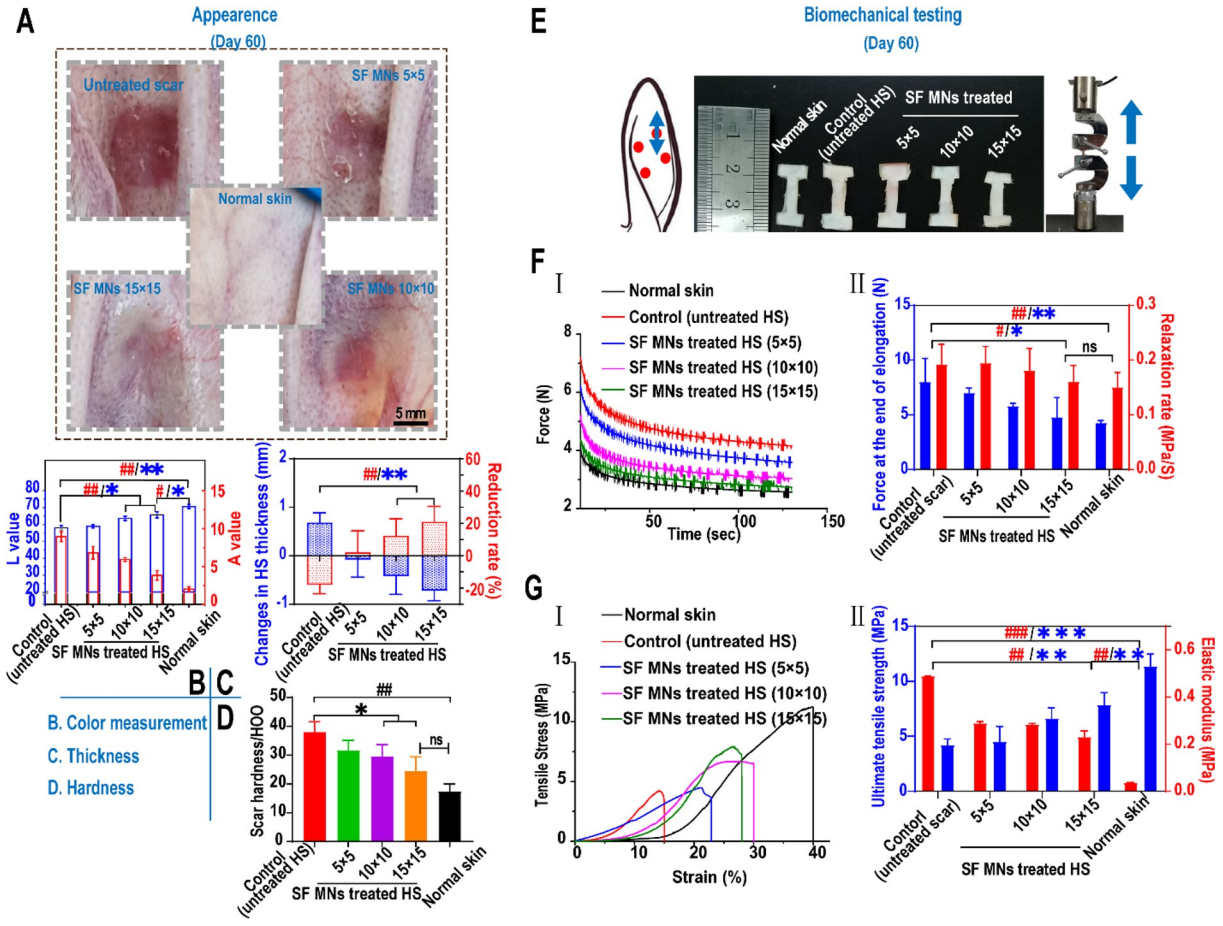

Figure 4. ***In vivo*** **treatment of rabbit ear hypertrophic scars with SF MN patches. (A) Appearances of post-treated scar tissues. Scale bar, 5 mm. (B) Color measurement of scars post-treatment. A higher value of L represents a whiter color, and a higher value of A represents a redder color. $^{**}p < 0.01$ and $^{*}p < 0.05$ represent significant differences in L values; $^{\#\#}p < 0.01$ represents significant differences in A value, $n = 3$. (C) Changes in thickness of scar tissues before and post-treatment. $^{**}p < 0.01$ represents significant differences in changes in thickness (mm); $^{\#\#}p < 0.01$ represents significant differences in the reduction rate of thickness (%), $n = 3$. (D) Hardness of scars post-treatment. $^{\#\#}p < 0.01$ compared with the normal dermis,; $^{*}p < 0.05$ compared with the control group, $n = 3$. (E) Dumbbell-shaped mechanical test specimens of uninjured skin and scars in the direction of the axial axis for the uniaxial stress relaxation and tensile failure testing. (F) In stress relaxation experiments, two measurements, including peak relaxation load and relaxation rate (II), were calculated from the elongation−relaxation data (I). $^{\#}p < 0.05$ represents a significant difference in the rate of relaxation; $^{*}p < 0.05$ represents a significant difference in peak load, $n = 3$. (G) Tensile failure experiments. Two measurements, including the ultimate tensile stress and elastic modulus (II), were calculated from stress−strain data (I). $^{\#\#\#}p < 0.001$ and $^{\#\#}p < 0.01$ represent significant differences in elastic modulus; $^{***}p < 0.001$ and $^{**}p < 0.01$ represent significant differences in ultimate tensile stress, $n = 3$.**

even after 30 days, which reflected a prolonged degradation with a controllable approach (Figure 2D).

Both silk fibroin and poly(vinyl alcohol) used for fabrication of MN patches exhibit excellent cytocompatibility. *In vitro*, there was no toxicity to cells while the fibroblasts were cocultured with MN extraction liquid produced by MNs' immersion into the medium for 2 weeks (Figure 2E). *In vivo*, no necrosis, congestion, or hemorrhage was found in the rabbit's heart, liver, spleen, lung, and kidney after 30 days of SF MN treatment, suggesting the patch's biocompatibility (Figure 2F).

Therapeutic Effects of a Silk Fibroin Microneedle Patch. The delayed healing of a full-thickness wound on the rabbit ear can lead to excessive collagen with disordered disposition, vascularization, and inflammation, which resembles a human hypertrophic scar.[40,48,49] Thus, we employed the rabbit ear model for this study. The time nodes of different stages of the whole experimental process are shown in Figure 3A. Four full-thickness wounds with a diameter of 1 cm were built on the ventral side of the rabbit ear. On day 28, HS models were proved to be established successfully (Figure 3B). Compared with the normal skin, elevated and red scars were observed, and significantly excessive and disordered collagen deposition was found from the hematoxylin and eosin (H&E) staining. The patches were then placed onto the scar tissues, and Figure 3C of the histological staining demonstrated that the MNs penetrated the scar and formed a hole of ~700 μm depth. The maximum thickness in parts of the scars was measured weekly. After one month, the HS tissues were harvested to measure hardness and color changes, for biomechanical testing, and for histology and biochemical analysis.

An HS has a different appearance from its adjacent normal skin in color and texture.[50] After one month of treatment, a significant improvement in the gross appearance of scars was seen, as shown in Figure 4A. As characterized in Figure 4B, the values of lightness (L: 65.7 ± 1.84) and redness (A: 3.83 ± 0.63) of an MN (15 × 15)-treated scar were very close to

https://doi.org/10.1021/acsnano.1c11016
ACS Nano 2022, 16, 10163−10178

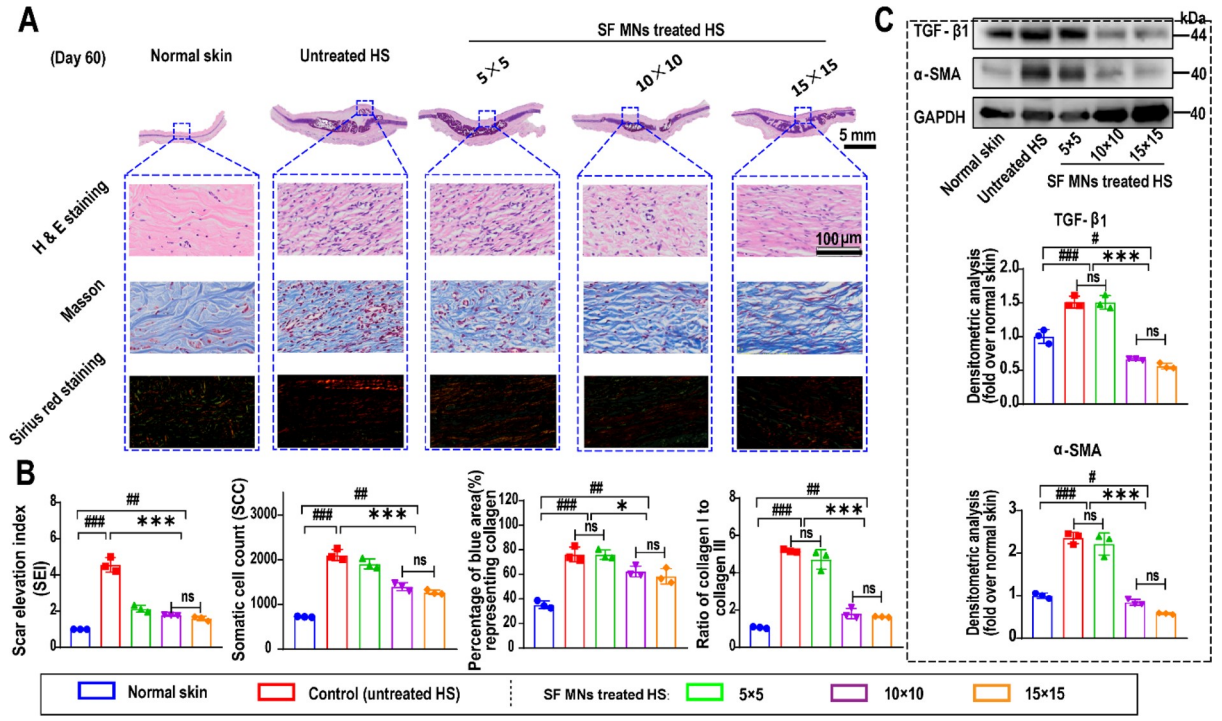

Figure 5. Histological analysis of the therapeutic effect of SF MNs. (A) Representative H&E, Masson, and Sirius red staining images of scar tissue and normal skin sections. Scale bar, 100 μm. (B) Quantification of SEI, cellularity, and collagen and ratio of type I to type III collagen from images in (A). (C) Western blotting analysis of TGF-β1 and α-SMA expression in scar tissues treated with different SF MN patches. Normal skin was used as a negative control. $^{###}p < 0.001$, $^{##}p < 0.01$, and $^{#}p < 0.05$ compared with normal skin and $^{***}p < 0.001$, $^{**}p < 0.01$, and $^{*}p < 0.05$ compared with the control group, $n = 3$.

normal skin (L: 70.7 ± 1.23, A: 2.02 ± 0.32), in contrast with the untreated scars (L: 58.03 ± 1.36, A: 8.94 ± 0.65). Besides, the thickness of the HS treated with a 15 × 15 patch decreased by an average of 0.72 mm with a reduction rate of 20.5 ± 0.5%. By contrast, in the untreated group, the thickness of scars gradually increased with an average increment rate of ∼18.1% (Figure 4C). The average reduction rate in the 5 × 5 and 10 × 10 groups was ∼3.2% and ∼13.2%, respectively. Similarly, there was a substantial decrease in the hardness of the SF MN-treated scars. As shown in Figure 4D, the hardness of the scar tissue in the MN treatment groups decreased 22.1% and 35.3%, respectively, for the 10 × 10 (29.6 ± 3.31 HOO, represents a Shore hardness of 29.6 as measured by a type HT-6510 OO Shore durometer) and 15 × 15 (24.6 ± 3.92 HOO) groups compared with the untreated scar (38 ± 2.90 HOO) (p = 0.018). There was no statistical differences between the 15 × 15 group and normal skin (17.4 ± 2.14 HOO) (p = 0.085). This suggested that the MN-induced physical intervention led to a noticeable improvement in the color of erythema and reductions of thickness, as well as a decreased hardness of scars.

Mechanical force and stress are crucial trigger factors that drive HS generation during wound healing.[5,8] Further study is necessary to reveal the biomechanical impacts on scar tissue in deformation resistance, load-bearing, and energy dissipation for a better understanding of the effects of SF MNs. As shown in Figure 4E, normal skin and scars were compared in uniaxial stress relaxation and tensile failure. In the uniaxial stress relaxation experiments, tissue specimens were subjected to 10% strain and then held for 120 s. Two measurements were conducted: the force generated during elongation and the rate of relaxation, which are indicative of a tissue's stiffness and viscous energy dissipation.[51] We found the force (8.02 ± 2.14 N) of the untreated HS occurred at 10% strain of elongation in contrast with 4.26 ± 0.22 N for normal skin, suggesting scar tissue displayed an even stiffer response to the given extension. However, the force of the MN-treated scars significantly declined, and the reduction extent responded to the increasing needle density of 5 × 5 (7.00 ± 0.45 N), 10 × 10 (5.81 ± 0.27 N), and 15 × 15 (4.79 ± 1.78 N). During relaxation, the untreated scar tissues showed more stress reduction per unit time (∼0.19 MPa/s) than normal skin (∼0.15 MPa/s). SF MN (15 × 15)-treated scars also experienced a slower stress relaxation rate of ∼0.16 MPa/s, which was close to normal skin (p = 0.64) (Figure 4F). We further conducted tensile testing to study the needle's impact on tissues' stiffness and strength during scar formation. The ultimate tensile strength was tested to indicate a tissue's ability to resist external stress.[52−55] As shown in Figure 4G, the untreated scar displayed the lowest maximum strain with the most insufficient tensile strength of 4.19 ± 0.45 MPa, compared with 11.37 ± 0.88 MPa for normal skin ($p < 0.01$). After MN treatment, the extensibility of scar tissue was improved, and the ultimate tensile stress in the 15 × 15 array reached 7.85 ± 0.78 MPa with almost a 2-fold increase ($p < 0.001$), although that treated HS had a significant difference from normal skin ($p < 0.01$). The scar tissue had a higher elastic modulus (∼0.489 MPa) than the normal skin (∼0.036 MPa). We found that the modulus decreased as the density of MNs increased, and the reduction of the elastic modulus in the 15 × 15 (∼0.23 MPa) group was more than 50% (Figure 4G, II). The improved ultimate strength and maximum extensibility of the HS suggest the MN intervention contributed to recovering the toughness and flexibility of injured skin.

https://doi.org/10.1021/acsnano.1c11016
ACS Nano 2022, 16, 10163−10178

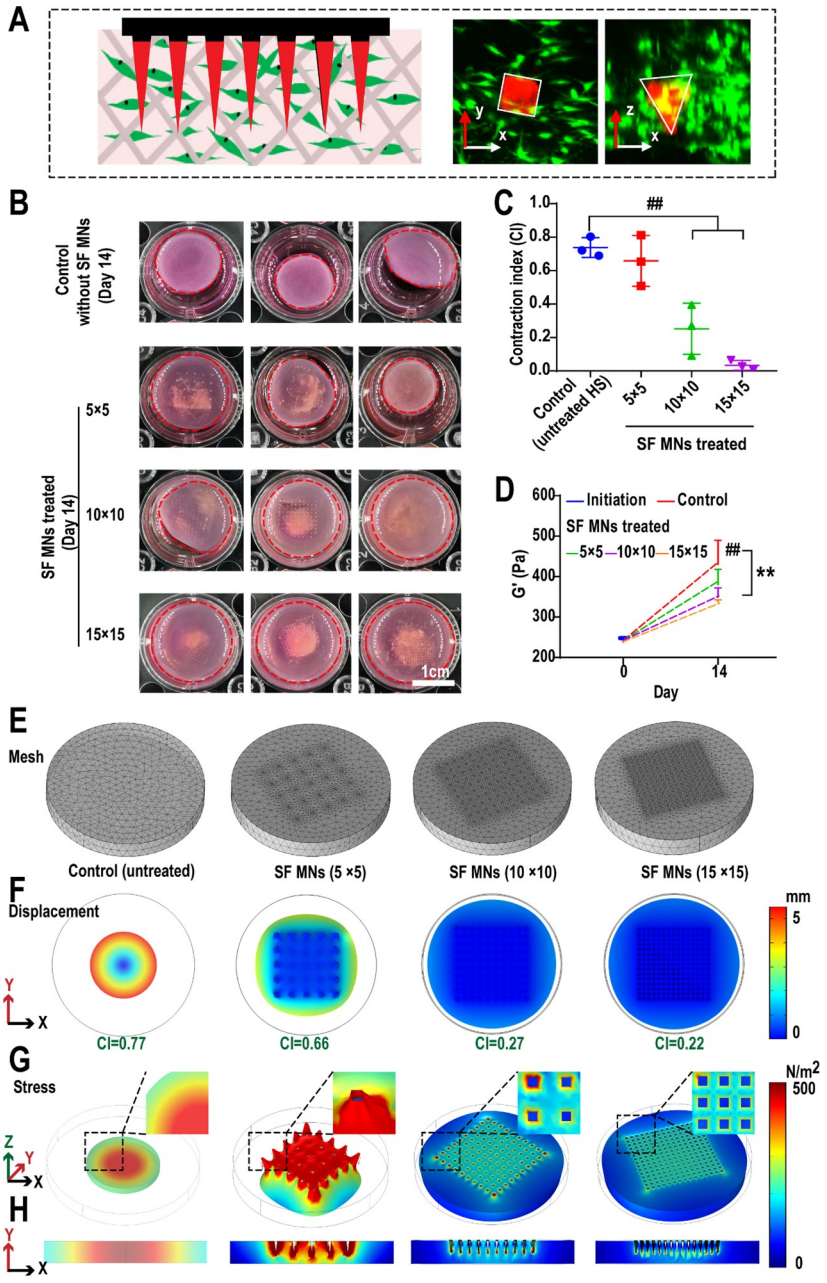

Figure 6. Experimental and simulation of SF MN patch induced mechanical impacts on collagen matrix deformation. (A) Schematic of the application of an SF MN patch in the FPCL system and confocal laser scanning microscopy images indicating the coexistence between fibroblasts and Cy-7-labeled SF MNs. (B–D) Tests of SF MN patch intervention inhibiting collagen matrix deformation; (B) fibroblast-generated contraction forcing the deformations of the collagen matrix; (C) contraction indexes (CIs) of the collagen matrix declining as the MN density increases ($^{\#\#}p < 0.01$, $n = 3$; scale bar, 1 cm); (D) storage modulus (G') of the 3D gel matrix significantly rising in proportion to the contraction ($^{**}p < 0.01$, $n = 3$). (E–H) Finite element simulation of the SF MN patch inducing a mechanical impact on collagen matrix deformation, (E) meshed FPCL system; (F) collagen contraction and the simulated CI; (G) 3D and (H) section contour of Von Mises stress.

In addition to the apparent morphology and mechanical properties, the therapeutic efficacy of SF MNs was further evaluated by studying the pathological features of HS tissue including excessive deposition of the ECM, increased cellularity, and chronic inflammation.[49,55] From section staining and Western blotting, we found that the elevated tissue and excessive collagen deposition were dramatically obvious (Figure 5A). The dermal thickness of HS tissues exceeded 2 mm, which was much thicker than normal skin (~0.4 mm). As shown in Figure 5B, the SEI was positively related to HS formation, but decreased from a maximum of 4.99 in untreated HS to a minimum of 1.45 after MN patch treatment (15 × 15). Also, the untreated scar showed the highest cellularity (more than 2100 cell/mm^2) of ~3-fold the normal dermis (~700 cell/mm^2). SF MN treatment reduced the somatic cell count (SCC) in the scar tissues gradually with increasing density of MNs (5 × 5: ~1900 cell/mm^2, 10 × 10: ~1400 cell/mm^2, 15 × 15: ~1300 cell/mm^2). Masson's trichrome staining indicated the excessive deposition and misalignment of collagen fibers in the untreated scar. The mean percentage of the blue area, which identified the collagen fibers, was 76.28% in the untreated scar, compared to 35.24%

https://doi.org/10.1021/acsnano.1c11016
ACS Nano 2022, 16, 10163–10178

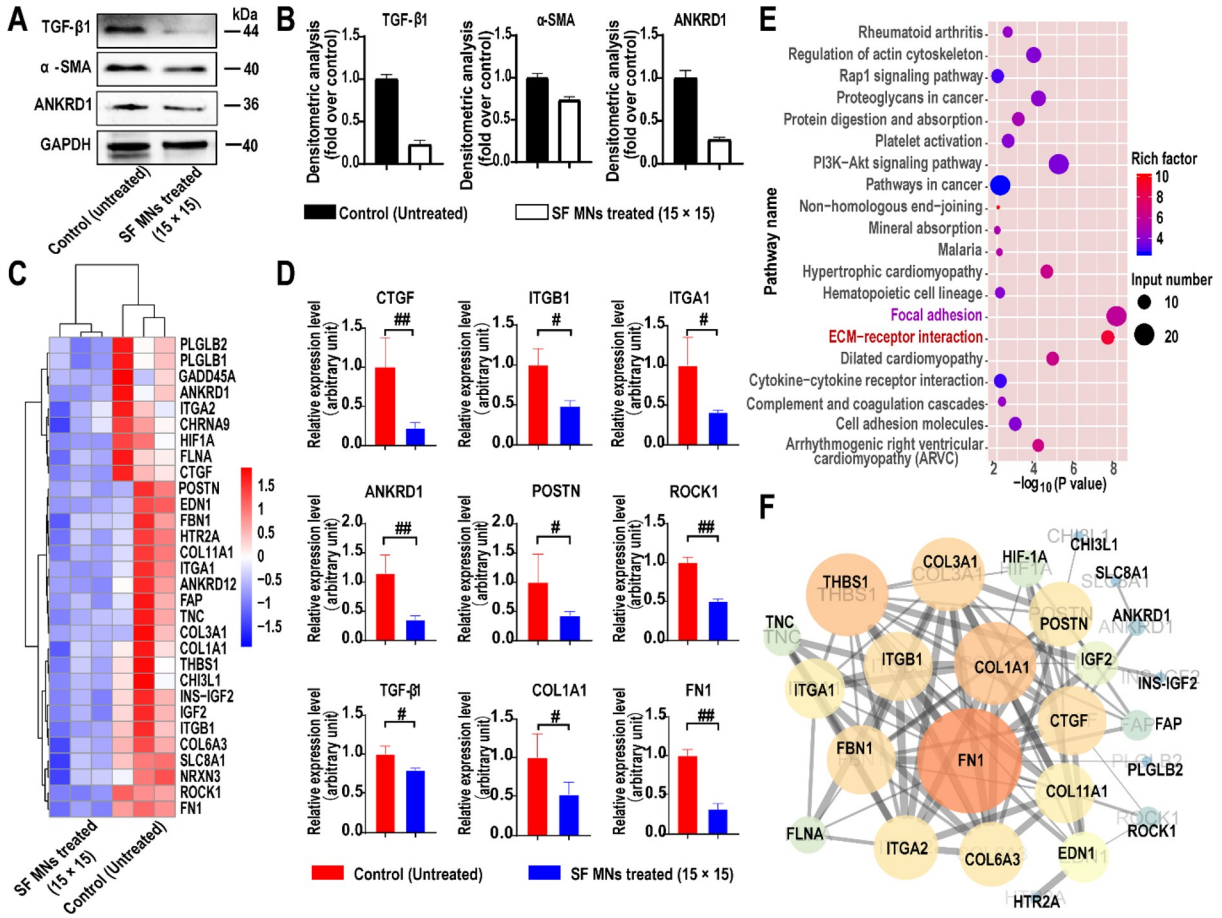

Figure 7. Cascade responses to SF MN-induced alteration of mechanical cues in the FPCL system. (A) Western blotting of TGF-β1, α-SMA, and ANKRD1. (B) Semiquantitative statistics of protein levels of (A), $p < 0.01$, $n = 3$. (C, D) Heat map and quantitative statistics of down-regulated genes involved in the cellular response to mechanical stimulus and the ECM in fibroblasts with SF MNs (fold change ≥ 4 and $p < 0.05$). (E) Kyoto Encyclopedia of Genes and Genomes (KEGG) pathway enrichment analysis based on the down-regulated genes. (F) Protein−protein interaction network of down-regulated genes involved in the ECM matrix and focal adhesion pathways.

in normal dermis ($p < 0.001$), and 76.07%, 62.31%, and 58.40% in groups of 5 × 5 ($p = 0.96$), 10 × 10 ($p = 0.032$), and 15 × 15 ($p = 0.023$), respectively. Additionally, type I and III collagen were further investigated by Sirius red staining. The results showed two different ratios of type I (red) to type III (green) collagen in the normal skin (approximately 1:1) and untreated HS tissues (approximately 5.18:1). In contrast, the ratio dropped dramatically to 1.64:1 in the HS response to treatment with 15 × 15 MNs ($p < 0.000\,01$ compared to untreated HS and $p < 0.01$ compared to normal skin) (Figure 5a and b). This indicated that SF MN treatments resulted in efficient inhibition of type I collagen, which is usually considered as the prominent part of the ECM of HSs.[56]

Considering that TGF-β1 and α-SMA play central roles in HS formation,[15,57] we examined the expression of TGF-β1 and α-SMA to further validate the scar-suppressing effects of SF MNs. As shown in Figure 5C, compared to the untreated group, the protein levels of TGF-β1 and α-SMA significantly diminished in the scar tissues of the MN patch treatment ($p < 0.001$). Even lower protein levels appeared in MN (15 × 15) treatment than normal tissues. It would be interesting to explore how these MNs mediated physical interventions connected to the down-regulation of fibrotic proteins and genes. Altogether, our finding suggests dramatic effects of SF MNs for HS treatment.

SF MN Patch Suppression of HSs *via* Mechanical Remodeling. Fibroblasts perceive the mechanical force from the surrounding microenvironment during wound healing and transfer the mechanical signal into the cell to prevent cellular apoptosis and promote ECM deposition, which possibly results in tissue fibrosis, a key inducement of hypertrophic scars.[5,8,24] To understand the underlying mechanisms of the SF MN patch on HSs, an FPCL was built to study the effects of SF MNs by simulating the contraction of human HS-derived fibroblasts (HSFs). The Cy-7-labeled SF MNs were embedded in the collagen matrix and cocultured with fibroblasts to demonstrate the prototype of the FPCL model (Figure 6A, Figure S3A). First, we confirmed that the SF solution itself had no notable inhibition effect on the HSF-induced collagen contraction at the concentration range from 5 to 20 mg/mL (Figure S3B) and also that the blank collagen gel (without fibroblasts) would not contract regardless of whether there is a microneedles patch (Figure S3C). However, we found that HSF-generated contraction can be effectively inhibited by the physical intervention of SF MNs (Figure 6B). As shown in Figure 6C, the contraction index (CI) was used to characterize the rate and the degree of matrix contraction. HSFs induced a strong contraction of the collagen matrix (the contraction rate was approximately 50%), and its contraction index reached 0.74. However, under the intervention of MNs, the collagen

https://doi.org/10.1021/acsnano.1c11016
ACS Nano 2022, 16, 10163−10178

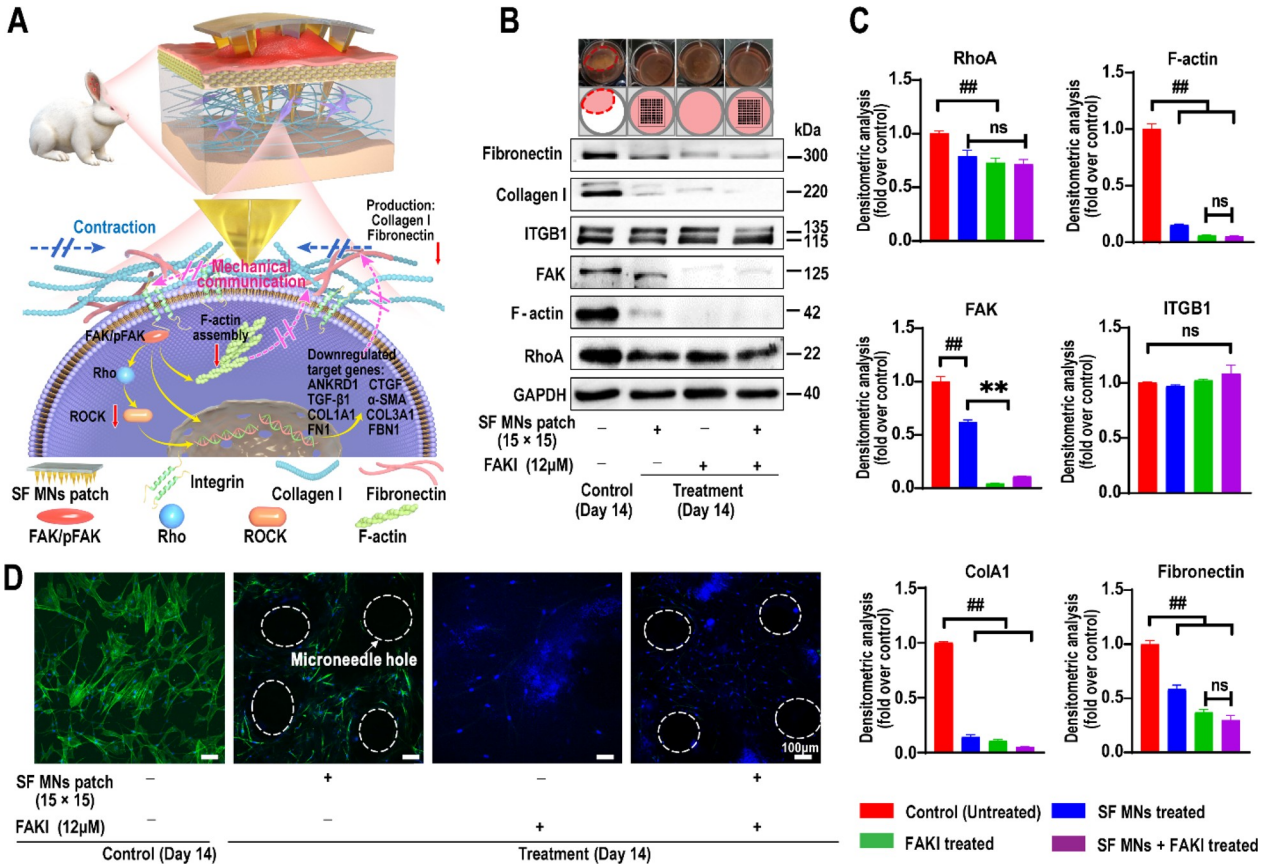

Figure 8. SF MNs alter the mechanical communication between fibroblasts and the surrounding matrix and result in a cascade of cellular responses. (A) Illustration of SF MN interrupting the mechanical communication between fibroblasts and the ECM to prevent fibroblast activation and promoting ECM remodeling with reduced secretions of collagen I and fibronectin *via* the integrin−FAK signaling pathway. (B) Western blotting of integrin, FAK, RhoA, and F-actin assembly, as well as type I collagen and fibronectin involved in the ECM network in fibroblasts with the treatment of FAKI, SF MNs, and FAKI + SF MNs. (C) Semiquantitative statistics of protein levels from Western blotting of (B). $^{\#\#}p < 0.001$, $n = 3$. (D) CLSM of the intracellular F-actin meshwork of fibroblasts under different treatments. Blue signals: nucleus; green signals: F-actin. Scale bar, 100 μm.

contraction rate declined with the increase in microneedle density, and the CIs of the collagen matrix in the 5 × 5 group (approximately 0.66), 10 × 10 group (about 0.25), and 15 × 15 group (around 0.03) were 89%, 34%, and 4.1% of the control group, respectively. Rheological analysis showed that the storage modulus G' of the collagen matrix with the interruption of SF MNs also dramatically changed. As shown in Figure 6D and Figure S4, the G' of the collagen matrix on day 0 was about 237 Pa. After 14 days of culture, the G' increased with the cell proliferation and contraction and reached ∼463.1 Pa in the control group. Nevertheless, the G' decreased with increasing the microneedle density (∼385 Pa in the 5 × 5 group, ∼349 Pa in the 10 × 10 group, ∼337 Pa in the 15 × 15 group, respectively); particularly, it was only 72.8% of the control group in the 15 × 15 group. The change in G' was consistent with the inhibition of SF MNs on the contraction. It is then necessary to characterize whether or not MNs induced a biomechanical shift in the collagen matrix. To advance the insight into the biomechanical process, we built a finite element model based on the experimental data of collagen deformation to numerically calculate the stress distribution in the collagen lattice in response to the SF MN intervention using COMSOL 5.6 (Figure 6E−H). We assumed that fibroblasts were homogeneously distributed in the collagen matrix. The collagen matrix was considered as a nonlinear viscoelastic material with a power-law dependence on stress.[58] The MNs embedded in collagen matrices were modeled as rigid. The simulation showed that the displacement of the collagen matrix along the *x*-, *y*-, and *z*-axes decreased gradually with the increased density of the MNs. The simulated CIs were close to the experimental ones, where simulated CI *versus* experimental CI was 0.77 *vs* 0.74 in the control, 0.66 *vs* 0.66 in the 5 × 5 array, 0.27 *vs* 0.25 in the 10 × 10array, and 0.22 *vs* 0.03 in the 15 × 15 array, respectively (Figure 6F), indicating that this model agreed perfectly with the actual FPCL model *in vitro*. Therefore, this model was then used to investigate how the intervention of MNs affected the stress field in the collagen matrix. Given the feedback loop of mechanical communication between cell−cell and cell−matrix, fibroblast-generated stress forced the volume deformation and stress stiffening of the collagen matrix, and in turn, the stiffer collagen matrix induced the fibroblasts to generate stronger forces.[59,60] Our simulation predicted that the stress in the collagen matrix decreased as the density of the MNs increased. As shown in Figure 6G and H, mechanical stress tends to concentrate in the center of the matrix during contraction in the control group. In contrast, the MN intervention induces the dispersion of stress, especially in the 10 × 10 and 15 × 15 groups. Besides, the mechanical stress level also decreased with MN treatment. However, on further study of the situations with increasing MN array density, the

https://doi.org/10.1021/acsnano.1c11016
ACS Nano 2022, 16, 10163−10178

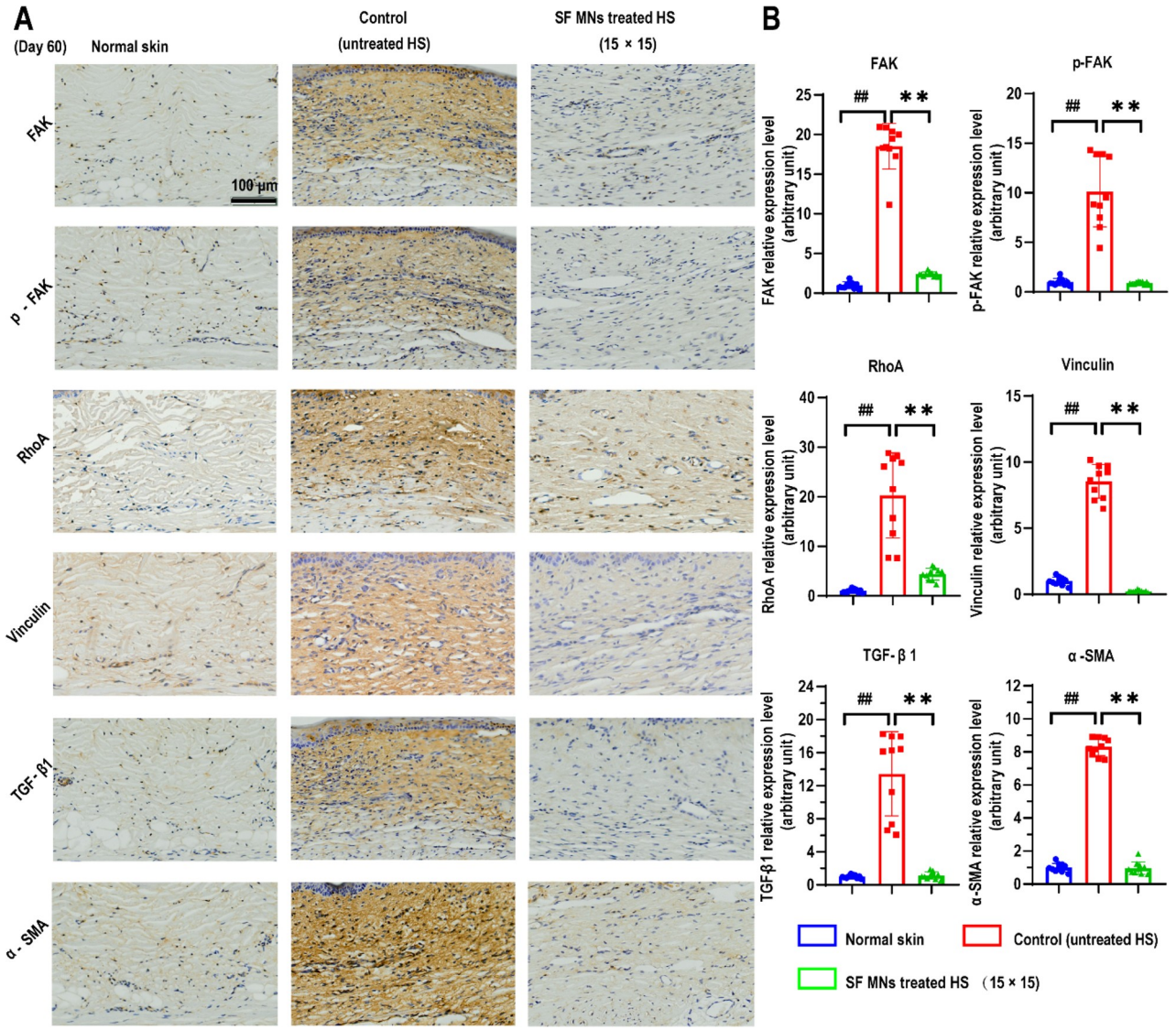

Figure 9. SF MN patch inhibiting the formation of hypertrophic scars *via* the integrin/FAK-mediated mechanotransduction signaling pathway. (A) Immunohistochemistry staining of FAK/pFAK, vinculin, RhoA, TGF-β1, and α-SMA. (B) Semiquantitative statistics of protein levels. $p < 0.0001$, $n = 10$. Scale bar, 100 μm.

contraction index marginally increased when the array density exceeded 20 × 20 (Figure S5). Additionally, higher mechanical stress tended to concentrate in areas of the needle tips with increasing array density. This might be because of the space compression caused by excessive array density, which would induce significant pressure on the collagen matrix and increased stress at the local contact sites. These results suggested that the embedded MNs impeded the collagen matrix's contraction and interfered with the collagen matrix mediated mechanical communication, resulting in reduced forces generated by fibroblasts. But it is worth noting that excess array density will not facilitate the subsequent mechanical remodeling response.

The expression of cytokines and proteins related to the mechanotransduction signaling pathway was also investigated. The weakened stress field was further identified by significant down-regulated expression of the mechanical sensitive gene ANKRD1 (Figure 7A and B), suggesting that fibroblasts perceived weaker mechanical force from the surrounding microenvironment[57] due to the SF MN intervention. As shown in Figure 7B, the protein concentration of TGF-β1 in the SF MN-treated group was only 0.26-fold that of the control group, and that of α-SMA was 0.73-fold that of the control. Therefore, we assumed that the mechanical force alteration under the physical intervention was an initial inducement of the therapeutic effect of SF MNs on HSs. Further contribution comes from the changes in related gene expression and cellular functions in response to the weakened mechanical stress during the pathological process of scarring.

To elucidate the transcriptomic changes associated with the blocked mechanical communications by SF MN intervention, we employed an experiment of RNA sequencing (RNA-seq). From the unguided principal component analysis, we found a significant difference between the transcriptomic profiles (Figure S6). As shown in the volcano plots, there were 126 up-regulated and 468 down-regulated genes in the treatment group compared to the control group according to the empirical Bayes method (fold change ≥ 4; $p < 0.05$). Specifically, multiple genes related to mechanotransduction (ANKRD1, ITGβ/α, and ROCK1) and scar formation

https://doi.org/10.1021/acsnano.1c11016
ACS Nano 2022, 16, 10163−10178

(COL1A1, COL3A1, HIF1A, CTGF, and FN1) were down-regulated after SF MN treatment (Figure 7C and D). A Kyoto Encyclopedia of Genes and Genomes (KEGG) pathway enrichment analysis revealed that the down-regulated genes were strikingly involved in the ECM matrix and focal adhesion pathways, reducing mechanotransduction and ECM deposition (Figure 7E). The protein−protein interaction network analysis identified the deposition of the ECM (COL1A1, COL3A1, COL6A3, COL11A1, FBN1, and FN1) was closely correlated with the cell-to-cell and cell-to-matrix (ITGβ/α, THBS1, ANKRD1, POSTN, and ROCK1) mechanical communication. Then, a cascade of signaling events occurred involving regulation of fibrosis-related gene expression, including CTGF, IGF2, and HIF1A (Figure 7F). These results suggested that the SF MNs triggered a cascade of negative regulation of scarring by weakening the mechanical stress in the environment.

The integrin−focal adhesion kinase (FAK) mediated mechanotransduction pathway takes part in transducing mechanical signals and the activation of fibroblasts in HS.[8,53] Moreover, compared to normal human dermal fibroblasts (HDFs), MN (15 × 15)-mediated intervention resulted in more significant changes in contraction and expression of pFAK, RhoA, and α-SMA in human scar fibroblasts (HSFs) (Figure S7). Therefore, we proposed that SF MNs might interrupt ECM-mediated mechanical communication and inhibit the activation of fibroblasts through the integrin−FAK pathway, resulting in reduced fibrosis (Figure 8A). In order to verify our assumption, we determined the expression of crucial proteins in this signaling pathway. As shown in Figure 8B, when the FAK inhibitor (FAKI, PF562271, 12 μM), the SF MN patch (15 × 15), or both of them were used, the contraction induced by active HSFs was significantly blocked, and the protein levels of FAK, RhoA, and F-actin were all dramatically down-regulated compared to the control group ($p < 0.01$) (Figure 8B and C). Consistent with Western blotting, we found that the untreated HSFs displayed stellate morphologies and were fully filled with an aligned actin meshwork (Figure 8D, green: F-actin assembly). However, HSFs with SF MNs displayed elongated cellular morphologies with less F-actin assemblies. Moreover, only very sparse actin networks were seen in the HSFs from FAKI with SF MNs. There was no significant difference between FAKI and FAKI with SF MNs, which reveals that SF MNs mainly attenuate FAK mechanotransduction to reduce the activation of fibroblasts. Due to the attenuated FAK mechanotransduction, our results also showed that both SF MN intervention and FAKI introduction induced statistically significant down-regulation of type I collagen (densitometry: mean gray values were less than 0.14-fold over the controls, $p < 0.000\,01$) and fibronectin (densitometry: mean gray values were less than 0.58-fold over the controls, $p < 0.0005$). Particularly, when we applied both MNs and FAKI stimuli simultaneously, there was no notable difference in protein levels between the MNs + FAKI group and the FAKI group (Figure 8B and D). These results indicated that the SF MNs could affect the structure of cytoskeletons and fibrous ECM protein composition by reducing intracellular mechanical signaling *via* the integrin−FAK pathway.

We then examined the protein levels related to mechanotransduction in scar tissue by immunofluorescence staining. *In vivo*, excessive deposition of ECM led to a stiffer scar tissue than normal tissue, resulting in activation of the focal adhesion pathways, containing FAK, vinculin, and other mechanosensing complex.[61] As shown in Figure 9A, the staining of FAK/p-FAK, vinculin, and RhoA was widely distributed in the whole scar section with a relatively high intensity in the untreated (control) group, but was barely distributed in the MN (15 × 15)-treated scars or normal tissues. The quantitative results showed that the relative expression level of FAK/p-FAK, vinculin, and RhoA in untreated scar tissue was almost 10 times or higher than those in normal dermis and SF MN patch (15 × 15) treated scars (Figure 9B), indicating that SF MNs relaxed the mechanical stress in scar tissue *via* a mild physical intervention approach with minimal invasiveness. Subsequently, the expressions of TGF-β1 and α-SMA were significantly down-regulated (Figure 9). Finally, our findings strongly support that the SF MNs can be an efficient approach to tune the biomechanics and ultrastructure of scar tissue and reconstitute a scar-free environment by inhibiting fibroblast-generated fibrosis and promoting extracellular matrix remodeling.

There is abundant evidence to support that abnormal mechanical stress drives cell behaviors of adhesion, migration, proliferation, and secretion, which are primary inducements for multiple diseases, such as atherosclerosis, fibrosis, pulmonary hypertension, inflammation, muscular dystrophy, and cancer.[11,21,23,55,62−64] Therefore, mechanical stimulation is also a crucial regulator that should not be ignored in tissue repair.[11] Consistent with the reported pathophysiological mechanism, mechanical stimulus can trigger abnormal ECM reconstruction, leading to HS formation. We hypothesized that polymeric MNs could physically interact with fibroblasts and the matrix to interfere with scar formation.

Silk fibroin-derived microneedles without payloads were used to test our hypothesis. We aimed at the mechanical signaling pathway, an entirely different perspective, to study the specific mechanism of polymeric microneedles involved in the minimally invasive treatment of HSs. A finite element simulation was conducted to verify the interaction prototype between the needles, matrix, and cells. We found that SF MNs can release the stress concentration by transforming a uniform and weak microenvironmental stress field around fibroblasts, verified by the down-regulated expression of the mechanical-sensitive gene ANKRD1 when MNs were introduced. The computational model was also used to predict the responses of collagen contraction and stress distribution as the MN array density increased. It suggested that increasing the array density was beneficial to mechanical microenvironment remodeling, but higher densities (≥20 × 20) did not always favor the remodeling. In terms of specific mechanisms, integrin−FAK-mediated mechanical signaling plays a central role in skin fibrosis and myofibroblast activation.[53,64] Fibroblasts perceive extracellular mechanical stress and convert it into intracellular profibrotic signals, resulting in the massive production of the ECM. In turn, excessive deposition of the ECM induces stiffer tissues and generates a higher mechanical force. In the integrin−FAK-mediated mechanotransduction signaling pathway, HSFs significantly down-regulated the F-actin assembly and adapted well to the weakened extracellular mechanical environment resulting from SF MN treatment. Meanwhile, the downstream secretion of collagen I and fibronectin substantially decreased, contributing to the remodeling of the low-stress microenvironment. Finally, the appearance and mechanical properties of scars were gradually improved and recovered *via* MN-mediated mechanotherapy. Consequently, this mecha-

https://doi.org/10.1021/acsnano.1c11016
ACS Nano 2022, 16, 10163−10178

notherapy approach is apparently different from the current microneedle-mediated HS therapeutic strategies (mainly transdermal drug delivery).[29,65,66]

Regulating local mechanical stress to alter scar outcomes has been an efficient approach to treating HSs, such as tension-reducing tapes and pressure garments. However, these existing long-term scar administrations still heavily depend on clinicians and their skills and are expensive.[15,25] Besides, the commercial tension-reducing tape is clinically used for linear scars, especially for scars after surgical incisions. It is mainly used to prevent scar formation by reducing tension around the linear incision.[67] But, in our study, rather than targeting the tension around a scar, we aimed to demonstrate that SF MN-induced physical intervention tends to reduce the mechanical communication in the ECM of scar tissue, thereby reconstituting a low-stress microenvironment that can benefit HS reversion. In addition to being applicable to linear surgical scars, the MN patch also shows better adaption on wide patchy scars than tension-reducing tapes. However, the physicochemical properties (such as geometry and materialogy) of MNs constantly cohering with circumstances of real morphology and thickness of scars and the results of clinical practices will need to be considered in our future research. As a minimally invasive option, this MN-mediated mechanotherapy strategy has great potential to provide cost-effective and convenient hypertrophic scar management for patients.

CONCLUSION

In conclusion, a microneedle patch made of biocompatible silk fibroin was demonstrated to ascertain its ability to inhibit hypertrophic scars *via* a minimally invasive approach without pain. The therapeutic mechanism was mainly attributed to the SF MNs' induced impediment of mechanical communication between fibroblasts and the ECM and reduction of fibroblast-generated mechanical stress. Furthermore, the attenuated integrin−FAK-mediated mechanical signaling led to a low-stress microenvironment to reduce scar formation. Overall, our results provided substantial results that SF MN intervention can be a promising self-management of HSs with a low-cost, effective, and convenient practice.

METHODS

Cell Lines and Animals. Primary HDFs and HSFs were isolated from human normal skin and pathological HSs, respectively, provided by the Institute of Burn Research in the Southwest Hospital of Army Medical University, Chongqing, China. Briefly, the excised skin tissue was washed with sterile phosphate-buffered saline (PBS). After removing the attached fat, the scar tissue was cut into small pieces and incubated continuously with 0.2% (w/v) collagenase type I and 0.25% pancreatin at 37 °C for 20 min. Cells were dissociated from enzyme-digested tissue and cultured in high-glucose Dulbecco's modified Eagle medium (DMEM; HyClone, South Logan, UT, USA) containing 10% fetal bovine serum (Gibco, USA) at 37 °C in 5% CO_2. For *in vitro* experiments, cells between passages 3 and 7 were used.

Healthy New Zealand rabbits were selected for animal experiments. The whole experiment was carried out according to the ethical approval agreement of the Ethics Committee of Army Military Medical University and the Guidelines for the Use of Experimental Animal Care (AMUWEC20192101).

Designing and Printing of a Positive Microneedle Master Mold. The positive MN master molds with arrays of 5 × 5, 10 × 10, and 15 × 15 were designed in an area of 1 cm × 1 cm using AutoCAD software. These pyramid-shaped needles had a base side length of 300 μm and a series of heights of 500, 1000, and 1500 μm. The designed master molds were printed using high-temperature-tolerating resin by a NanoArch S140 3D printer (BMF Material Technology Inc.).

Fabrication of the Negative PDMS Microneedle Mold. The master microneedle molds were dip-coated with 1% PVA solution and dried in an oven to facilitate demolding. Then, PDMS (Sylgard 184) was mixed with a curing agent at a ratio of 10:1, cast in the positive microneedle master molds, and placed in a vacuum oven at 80 °C for 2 h. After demolding, the negative silicone microneedle molds were obtained.

Fabrication of Silk Fibroin Microneedle Patches. To fabricate the SF microneedle patches, the PDMS negative molds were first treated with O_2 plasma to improve the surface hydrophilicity, allowing the SF solution to be filled in the microcavities. Silk fibroin protein extracted from *Bombyxmori* cocoons (Simatech, Jiangsu, China) was dissolved in deionized water to prepare an aqueous SF solution (10%, w/v) and cast into the pretreated molds, and excess fluid was removed. After gelation at 4 °C, the solid-state SF was dried overnight in a vacuum (60 °C) oven filled with methanol to obtain a high content of beta-sheet secondary structure, which contributes to the higher mechanical strength of the SF MNs.[43] Next, an aqueous PVA solution (15%, w/v, MW = 80 kDa) was poured onto the mold to form a flexible backing substrate. After completely forming, the MN patches with the PVA substrate were carefully separated from the PDMS negative mold and sterilized with epoxyethane (55 °C, 1 h) under vacuum before use.

Morphology Observation of SF MN Patches. A Leica digital camera took a digital photo of each SF MN patch. The SEM images were captured by a Zeiss Gemini SEM 300 instrument (Zeiss, Germany).

Mechanical Characterization. The mechanical performance of microneedles was determined by pressing a stainless-steel plate against the microneedles on an MTS E44 universal tester with a 100 N compression load cell. When the upper plate initially touched the microneedle tips, the distance between the upper and lower plate was zero. The lower plate moved upward to the MN patch at a constant 0.1 mm/min speed until the needles buckled and broke. The compressive force was recorded, and the yield stress of a single needle was calculated by the following formula:[65]

$$\sigma = \frac{F}{S}$$

where σ represents the yield stress, F represents the compression force (total force/numbers of needles), and S represents the bottom $x-y$ sectional area of a single needle.

Fourier Transform Infrared Spectroscopy Analysis. The microneedles were cut off and collected from 10 patches for FTIR testing (Shimadzu Spectrum 400 FTIR, Japan). To analyze the secondary structures of the SF MNs, the primary spectra (1600−1700 cm^{-1}) of amide I were deconvoluted by a secondary derivative method using the Peakfit 4.12 software.

Contact Angle Measurements. Quantification of contact angles of 10% aqueous collagen (originating from rat tail) on different density MN arrays was performed by an optical contact angle meter and interface tensiometer (SL 150E, KINO Industry Limited, USA).

Swelling Ratio Determination. The SF MN patches were inserted into a piece of fresh porcine skin and allowed to stand in a vacuum vessel. At the desired time point, the MN patches were taken out, and the tissue debris was gently removed from the surface. The patch's weight before (W_{dry}) and after experiment (W_{swell}) was recorded. The swelling ratio can be calculated by the following formula:

$$\text{Swelling ratio } (\%) = \frac{W_{swell} - W_{dry}}{W_{dry}} \times 100\%$$

***In Vivo* Degradation of SF Microneedles.** The SF MN patches were inserted into the hypertrophic scars of rabbit ears. After penetration for a certain time (3, 7, 20, and 30 days), the MN patches were withdrawn and observed by SEM (Zeiss Sigma 300, Germany)

https://doi.org/10.1021/acsnano.1c11016
ACS Nano 2022, 16, 10163−10178

and a DVM6 digital microscope with LAS X software from Leica microsystems (Leica DVM6, Germany).

Biocompatibility of SF Microneedles. The biocompatibility of the SF MN patch was assessed by the cell viability of fibroblasts and sections of visceral organs. Briefly, *in vitro*, sterile SF MN patches were immersed in complete DMEM (1 MN patch/mL DMEM) for 2 weeks and then filtered (0.22 μm) to obtain the extract of the MN patches. Then, fibroblasts were incubated in a 12-well plate (2×10^5/well) with 1 mL of extract in each well (one SF MN patch equivalent) for a preconceived time, which was consistent with the situation of one SF MN patch per well in the FPCL model. The cytotoxicity of sterile extracts of microneedles to fibroblasts was determined by the CCK8 method. *In vivo*, sterile SF MNs penetrated into the scar tissues for 30 days. After the rabbit was sacrificed, the degree of necrosis, congestion, and hemorrhage of the heart, liver, spleen, lung, and kidney was observed by pathological sectioning.

Fibroblast-Populated Collagen Lattice System. The soluble type I collagen was extracted from the rat tail. Briefly, the tails of SD rats of about 250 g were cut off and immersed in 75% alcohol for 20 min. Four tendons were extracted from the tail and cut into pieces under aseptic conditions. After the tendons were dissolved in 0.5% acetic acid solution (100 mL/tail) at 4 °C for 3 days, the supernatant was separated by centrifugation (12 000 rpm, 4 °C) and salted out using 10% NaCl solution. The obtained collagen was then dissolved in 1 mM HCl to prepare a collagen solution at a 20 mg/mL concentration and stored at 4 °C before use.

To make a three-dimensional culture system of an FPCL, first, rat tail collagen was mixed with 1 M NaOH solution and adjusted to pH 7.4. Then, the collagen was mixed with complete DMEM (containing 10% fetal bovine serum) and a cell suspension (1×10^6 cells/mL) at a volume ratio of 7:2:1. The mixture was added into a 12-well plate to form a gel after 30 min in the incubator and incubated with 1 mL of complete DMEM for 3 days. Then the medium was replaced by DMEM without fetal bovine serum and incubated for another 3 days. Next, the FPCLs were treated with or without SF MN patches (arrays of 5 × 5, 10 × 10, 15 × 15) and allowed to stand for more than 5 days until the diameter of the FPCL no longer changed obviously. Finally, the diameters were quantified *via* ImageJ, and the contraction index was calculated as follows:

$$\mathrm{CI} = 1 - \left(\frac{A}{A_0}\right)^2$$

where A represents the quantified area of the collagen gel at the end of the experiment and A_0 represents the initial area of the collagen gel.

To visualize F-actin formation, fibroblasts in the collagen lattice were first fixed with 1% paraformaldehyde for 30 min and then permeabilized with 0.1% Triton-100 in PBS for 1 h. Afterward, the cell nucleus and F-actin were stained with 4′,6-diamidino-2-phenylindole (DAPI, Beyotime, China) and Alexa Fluor 488 phalloidin (1:500, Thermo Fischer Scientific, USA) for 15 min, respectively. Finally, the fluorescent cytoarchitecture was imaged by a confocal microscope (SpinSR10, Olympus, Japan).

Finite Element Analysis. A finite element analysis model in COMSOL 5.6 (COMSOL Inc., Sweden) was established for the simulation of structural mechanics of the gel matrix response to the insertion of MNs.[9,68] The gel matrix was modeled as a homogeneous and nonlinear elastic material with an elastic modulus ($E = 2G'(1 + \upsilon)$) of 746 Pa and Poisson's ratio (υ) of 0.3,[58] and a hypothesis of free displacement was applied as the boundary conditions of the collagen matrix. Three arrays (5 × 5, 10 × 10, 15 × 15) of SF MN patches were modeled, and the pyramid-shaped MNs (height of 1000 μm) were considered as rigid geometries under a displacement constraint where u_x and u_y are considered null. The geometrical structures of the collagen matrix and microneedles were set to form a "union", and there was no sliding between the contact boundaries. Meanwhile, a hyperfine free tetrahedral mesh (the maximum and minimum mesh sizes are 70 and 3 μm) approach was used to ensure accurate results.

RNA Sequencing Analysis. The changes in gene expression of fibroblasts after being treated with or without an SF MN patch in the FPCL system were quantified using second-generation sequencing technology. The fibroblasts were harvested after the extracellular collagen lattice was hydrolyzed by 0.2% (w/v) collagenase type I. Then, total RNAs were extracted from HSFs using TRIzol reagent and used for stranded RNA sequencing. The RNA sequencing library products corresponding to 200−500 bps were enriched, quantified, and finally sequenced on the Novaseq 6000 sequencer (Illumina) with the PE150 model.

Animal Model of a Hypertrophic Scar. The *in vivo* hypertrophic scar model was established on the ventral side of the rabbit ear according to the previously reported method with modification.[48] Briefly, four full-thickness skin resections (1 cm in diameter) were created on each ear, and the perichondrium on the base of the wound was completely removed using a scalpel. The scabs were ripped off repeatedly to delay re-epithelialization and to promote the hyperostosis of granulation and fibroplasia, which led to a raised scar. Thirty days postsurgery, the wound was completely healed and formed a hypertrophic scar.[65]

***In Vivo* SF MN Patch Interventional Treatment.** The therapeutic effects of the SF MN patch were performed in a rabbit ear hypertrophic scar model. SF MN patches with different density arrays of 5 × 5, 10 × 10, and 15 × 15 were applied to penetrate the HS tissues and held in place for 4 weeks. The SF MN patches were taken out on the day before tissue sampling, the thickness, hardness, and colors of scars were measured using a vernier calliper, Shore durometer (Shore, HT-6510OO, Guangzhou Landtek Instrument Co., Ltd, China), and MiniScan XE Plus spectrocolorimeter (HunterLab, Reston, VA, USA), respectively.

Biomechanical Testing. Before mechanical testing, as described previously,[51,53,69] the test specimens were carefully collected from both uninjured dermis and scars in the axial axis (tip to posterior of rabbit ear) and dumbbell-shaped via scalpel. The specimens' length, thickness, and width were then measured manually using a vernier caliper (0.01 mm). Then, the ends of the dumbbell-shaped geometry were wrapped in gauze to ensure that the specimens were tightly clamped by upper and lower grips and vertically secured in the MTS machine (Meitesi Testing Technology Co., Ltd., Jinan, China).

For stress relaxation, specimens were elongated 1.0 mm (approximately 10% of the gauge length) at a constant rate of 0.1 mm/s and held for 120 s, and the force−time curve was recorded and fitted using a power-law formulation as follows:

$$f(x) = ax^{-b}$$

where x represents the time of retention, a represents the magnitude of the force, and b is the rate of relaxation.

For tensile failure, specimens were stretched at a constant rate of 1 mm/s until failure. The ultimate tensile strength was recorded.

Histological and Immunofluorescent Assays. Specimens were harvested and fixed in 4% paraformaldehyde, dehydrated, and then paraffin-embedded and cut at a thickness of 5 μm. H&E, Masson's trichrome, and Sirius red staining was performed according to routine protocols. The images were photographed with microscope and polarizer accessories and quantified using ImageJ. The scar elevation index, which can be referred to as the ratio of the total tissue thickness of scar tissue to that of normal tissue above the cartilage surface, was calculated as follows to quantify the degree of scarring.[65,70]

$$\mathrm{SEI} = \frac{T_{\mathrm{scar}}}{T_{\mathrm{normal}}}$$

where T_{scar} represents the maximum thickness of the scar tissue and T_{normal} represents the maximum thickness of normal dermis around the scar tissue, which was measured from the top point of the epithelium to the surface of the cartilage in the scar and normal tissue, respectively.

In the immunohistochemistry assay, tissue sections were incubated with primary antibody against FAK (Bioss, bs-20735R, 1:500), p-FAK (phosphor Ser732, Bioss, bs-1642R, 1:500), RhoA (Bioss, bs-22249R, 1:500), vinculin, (Abcam, ab178698, 1:100), and TGF-β1 (Abcam, ab92486, 1:100), α-SMA (Abcam, ab5694, 1:100) diluted in blocking

https://doi.org/10.1021/acsnano.1c11016
ACS Nano 2022, 16, 10163−10178

solution overnight at 4 °C. After being incubated with HRP-conjugated secondary antibody, the sections were counterstained with hematoxylin and developed with diaminobenzidine. The percentage of targeting protein was quantified using ImageJ.

Western Blotting. The Western blotting assay was performed according to the standard protocol as previously reported.[57] Scar tissues or HFs cultured in FPLC were lysed with RIPA buffer supplied with protease inhibitor cocktail (Beyotime, P0013C, China). Concentrations of total protein were detected by the bicinchoninic acid (BCA) assay (Beyotime). The separated proteins were immunoblotted with primary anti-GAPDH (CST, #5174, 1:1000), anti-FAK (Abcam, ab40794, 1:1000), anti-pFAK (phosphoS732) antibody (Abcam, ab4792, 1:500), anti-RhoA antibody (CST, #2117, 1:1000), anticollagen type I (CST, #72026,1:1000), anti-fibronectin/FN1 (CST, #26836, 1:1000), anti-integrin β1 antibody (CST, #34971, 1:1000), and anti-ANKRD1 antibody (ab134543, Abcam, 1:500) at 4 °C overnight The signals of protein bands were imaged by automatic chemiluminescence image analysis system (Invitrogen iBright 1500, Thermo Fisher) and analyzed using ImageJ software.

Statistical Analysis. All the quantitative values were expressed as the mean ± standard deviations (SD). Statistical analysis was carried out using the *t* test with GraphPad Prism (GraphPad Software 8.0.1), while the value of $p < 0.05$ was considered a statistically significant difference between groups.

ASSOCIATED CONTENT

Supporting Information

The Supporting Information is available free of charge at https://pubs.acs.org/doi/10.1021/acsnano.1c11016.

Preparation of PDMS mold; length effects of microneedles on therapeutic efficacy; optical microscope and laser scanning microscope of the FPCL system; HSF-derived fibroblasts generated collagen contraction; modulus of the collagen hydrogel in FPCL; changes in contraction and expression of pFAK, RhoA, and α-SMA in normal HDFs and HSFs; finite element analysis of the interaction between MNs and collagen gels; principal component analysis and volcano plots of RNA sequencing analysis; secondary structure composition of natural SF and methanol-treated SF (PDF)

AUTHOR INFORMATION

Corresponding Authors

Jianglin Tan − *Institute of Burn Research, State Key Laboratory of Trauma, Burn and Combined Injury, Southwest Hospital, Third Military Medical University (Army Medical University), Chongqing 400038, China*; Email: jianglintan@aliyun.com

Malcolm Xing − *Department of Mechanical Engineering, University of Manitoba, Winnipeg R3T 2N2, Canada*; orcid.org/0000-0002-3547-0462; Email: malcolm.xing@umanitoba.ca

Gaoxing Luo − *Institute of Burn Research, State Key Laboratory of Trauma, Burn and Combined Injury, Southwest Hospital, Third Military Medical University (Army Medical University), Chongqing 400038, China*; orcid.org/0000-0003-4764-3209; Email: logxw@tmmu.edu.cn

Authors

Qing Zhang − *Institute of Burn Research, State Key Laboratory of Trauma, Burn and Combined Injury, Southwest Hospital, Third Military Medical University (Army Medical University), Chongqing 400038, China*; orcid.org/0000-0002-4698-0193

Lin Shi − *Institute of Burn Research, State Key Laboratory of Trauma, Burn and Combined Injury, Southwest Hospital, Third Military Medical University (Army Medical University), Chongqing 400038, China*

Hong He − *Ministry of Education & Key Disciplines Laboratory of Novel Micro-Nano Devices and System Technology, Chongqing University, Chongqing 400044, China*

Xingmou Liu − *Institute of Burn Research, State Key Laboratory of Trauma, Burn and Combined Injury, Southwest Hospital, Third Military Medical University (Army Medical University), Chongqing 400038, China; Chongqing Key Laboratory of Complex Systems and Bionic Control, Chongqing University of Posts and Telecommunications, Chongqing 400065, China*

Yong Huang − *Institute of Burn Research, State Key Laboratory of Trauma, Burn and Combined Injury, Southwest Hospital, Third Military Medical University (Army Medical University), Chongqing 400038, China*

Dan Xu − *Department of Pathology, Southwest Hospital, Third Military Medical University (Army Medical University), Chongqing 400038, China*

Mengyun Yao − *Institute of Burn Research, State Key Laboratory of Trauma, Burn and Combined Injury, Southwest Hospital, Third Military Medical University (Army Medical University), Chongqing 400038, China*

Ning Zhang − *Institute of Burn Research, State Key Laboratory of Trauma, Burn and Combined Injury, Southwest Hospital, Third Military Medical University (Army Medical University), Chongqing 400038, China*

Yicheng Guo − *Institute of Burn Research, State Key Laboratory of Trauma, Burn and Combined Injury, Southwest Hospital, Third Military Medical University (Army Medical University), Chongqing 400038, China*

Yifei Lu − *Institute of Burn Research, State Key Laboratory of Trauma, Burn and Combined Injury, Southwest Hospital, Third Military Medical University (Army Medical University), Chongqing 400038, China*

Haisheng Li − *Institute of Burn Research, State Key Laboratory of Trauma, Burn and Combined Injury, Southwest Hospital, Third Military Medical University (Army Medical University), Chongqing 400038, China*

Junyi Zhou − *Institute of Burn Research, State Key Laboratory of Trauma, Burn and Combined Injury, Southwest Hospital, Third Military Medical University (Army Medical University), Chongqing 400038, China*

Complete contact information is available at: https://pubs.acs.org/10.1021/acsnano.1c11016

Author Contributions

Q.Z. conceived, designed, and conducted the experiments, with suggestions from J.T., M.X., and G.L.; Q.Z. performed the preparation and characterization of the SF MN patches; Q.Z. and L.S. performed the cellular experiments and animal experiments with the help of J.T., M.Y., N.Z., Y.L., H.L., and J.Z.; Q.Z. performed the finite element analysis, with the help of H.H. and M.L.; Y.H. and D.X. prepared histopathologic sections; Q.Z. and J.T. wrote, revised, and corrected the manuscript, with the help of M.X., G.L., and Y.G.

Notes

The authors declare no competing financial interest.

https://doi.org/10.1021/acsnano.1c11016
ACS Nano 2022, 16, 10163−10178

ACKNOWLEDGMENTS

We thank Z. Gu for suggestions on our experiments; the graduate student J. Z. Li for providing human hypertrophic scar fibroblasts; and X. R. Zhang for experiments of Western blotting. The authors gratefully acknowledge financial support from the National Key R&D Program of China, 2021YFA1101100 (G.L.); China Postdoctoral Science Foundation, 2019M653979 (Q.Z.); and National Natural Science Foundation of China, 82072188 (J.T.).

REFERENCES

(1) Finnerty, C. C.; Jeschke, M. G.; Branski, L. K.; Barret, J. P.; Dziewulski, P.; Herndon, D. N. Hypertrophic Scarring: The Greatest Unmet Challenge after Burn Injury. *Lancet* **2016**, *388*, 1427−1436.
(2) Sofroniew, M. V. Inflammation Drives Fibrotic Scars in The CNS. *Nat. Neurosci.* **2021**, *24*, 155−159.
(3) Lim, G. B. Macrophages Produce Collagen for Myocardial Scar Formation. *Nat. Rev. Cardiol.* **2020**, *17*, 267.
(4) Jiang, D.; Correa-Gallegos, D.; Christ, S.; Stefanska, A.; Liu, J.; Ramesh, P.; Rajendran, V.; De Santis, M. M.; Wagner, D. E.; Rinkevich, Y. Two Succeeding Fibroblastic Lineages Drive Dermal Development and The Transition From Regeneration to Scarring. *Nat. Cell Biol.* **2018**, *20*, 422−431.
(5) Mascharak, S.; desJardins-Park, H. E.; Davitt, M. F.; Griffin, M.; Borrelli, M. R.; Moore, A. L.; Chen, K.; Duoto, B.; Chinta, M.; Foster, D. S.; et al. Preventing Engrailed-1 Activation in Fibroblasts Yields Wound Regeneration Without Scarring. *Science* **2021**, *372*, 346−357.
(6) Konieczny, P.; Naik, S. Healing Without Scarring. *Science* **2021**, *372*, 346−347.
(7) Lee, H.; Thuret, S. Adult Human Hippocampal Neurogenesis: Controversy and Evidence. *Trends Mol. Med.* **2018**, *24*, 521−522.
(8) Barnes, L. A.; Marshall, C. D.; Leavitt, T.; Hu, M. S.; Moore, A. L.; Gonzalez, J. G.; Longaker, M. T.; Gurtner, G. C. Mechanical Forces in Cutaneous Wound Healing: Emerging Therapies to Minimize Scar Formation. *Adv. Wound Care (New Rochelle)* **2018**, *7*, 47−56.
(9) Cheng, L.; Sun, X.; Yu, J.; Guo, Q.; Jin, R.; Sun, B.; Shi, Y.; Cui, W.; Zhang, Y. A Facilely Fabricated *in vivo* Hypertrophic Scar Model Through Continuous Gradient Elastic Tension. *RSC Adv.* **2015**, *5*, 107430−107444.
(10) Ghosh, B.; Mandal, M.; Mitra, P.; Chatterjee, J. Structural Mechanics Modeling Reveals Stress-adaptive Features of Cutaneous Scars. *Biomech. Model. Mechanobiol.* **2021**, *20*, 371−377.
(11) Montagner, M.; Dupont, S. Mechanical Forces as Determinants of Disseminated Metastatic Cell Fate. *Cells* **2020**, *9*, 250−271.
(12) He, J.; Fang, B.; Shan, S.; Xie, Y.; Wang, C.; Zhang, Y.; Zhang, X.; Li, Q. Mechanical Stretch Promotes Hypertrophic Scar Formation Through Mechanically Activated Cation Channel Piezo1. *Cell Death Dis.* **2021**, *12*, 226−239.
(13) Durant, F.; Whited, J. L. Finding Solutions for Fibrosis: Understanding the Innate Mechanisms Used by Super-Regenerator Vertebrates to Combat Scarring. *Adv. Sci. (Weinh)* **2021**, *8*, 2100407.
(14) Stoica, A. E.; Grumezescu, A. M.; Hermenean, A. O.; Andronescu, E.; Vasile, B. S. Scar-Free Healing: Current Concepts and Future Perspectives. *Nanomaterials (Basel)* **2020**, *10*, 2179−2197.
(15) Coentro, J. Q.; Pugliese, E.; Hanley, G.; Raghunath, M.; Zeugolis, D. I. Current and Upcoming Therapies to Modulate Skin Scarring and Fibrosis. *Adv. Drug Delivery. Rev.* **2019**, *146*, 37−59.
(16) Li, J.; Cen, B.; Chen, S.; He, Y. MicroRNA-29b Inhibits TGF-beta1-induced Fibrosis *via* Regulation of The TGF-beta1/Smad Pathway in Primary Human Endometrial Stromal Cells. *Mol. Med. Rep.* **2016**, *13*, 4229−4237.
(17) Sriram, S.; Gibson, D.; Robinson, P.; Tuli, S.; Lewin, A. S.; Schultz, G. Reduction of Corneal Scarring in Rabbits by Targeting The TGFB1 Pathway With A Triple siRNA Combination. *Adv. Biosci. Biotechnol.* **2013**, *04*, 47−55.
(18) Zhao, R.; Yan, Q.; Huang, H.; Lv, J.; Ma, W. Transdermal siRNA-TGFbeta1−337 Patch for Hypertrophic Scar Treatment. *Matrix Biol.* **2013**, *32*, 265−276.
(19) Tan, J.; Wu, J. Current Progress in Understanding The Molecular Pathogenesis of Burn Scar Contracture. *Burns Trauma* **2017**, *5*, 14.
(20) Vermeulen, S.; Roumans, N.; Honig, F.; Carlier, A.; Hebels, D. G. A. J.; Eren, A. D.; Dijke, P. t.; Vasilevich, A.; de Boer, J. Mechanotransduction Is A Context-dependent Activator of TGF-β Signaling in Mesenchymal Stem Cells. *Biomaterials* **2020**, *259*, 120331.
(21) Romani, P.; Valcarcel-Jimenez, L.; Frezza, C.; Dupont, S. Crosstalk Between Mechanotransduction and Metabolism. *Nat. Rev. Mol. Cell Biol.* **2021**, *22*, 22−38.
(22) Wong, V. W.; Rustad, K. C.; Akaishi, S.; Sorkin, M.; Glotzbach, J. P.; Januszyk, M.; Nelson, E. R.; Levi, K.; Paterno, J.; Vial, I. N.; et al. Focal Adhesion Kinase Links Mechanical Force to Skin fibrosis *via* Inflammatory Signaling. *Nat. Med.* **2012**, *18*, 148−152.
(23) Wong, V. W.; Paterno, J.; Sorkin, M.; Glotzbach, J. P.; Levi, K.; Januszyk, M.; Rustad, K. C.; Longaker, M. T.; Gurtner, G. C. Mechanical Force Prolongs Acute Inflammation *via* T-cell-Dependent Pathways During Scar Formation. *FASEB J.* **2011**, *25*, 4498−4510.
(24) Stewart, L.; Turner, N. A. Channelling the Force to Reprogram the Matrix: Mechanosensitive Ion Channels in Cardiac Fibroblasts. *Cells* **2021**, *10*, 990−1024.
(25) Mokos, Z. B.; Jovic, A.; Grgurevic, L.; Dumic-Cule, I.; Kostovic, K.; Ceovic, R.; Marinovic, B. Current Therapeutic Approach to Hypertrophic Scars. *Front. Med. (Lausanne)* **2017**, *4*, 83−94.
(26) Klifto, K. M.; Asif, M.; Hultman, C. S. Laser Management of Hypertrophic Burn Scars: a Comprehensive Review. *Burns Trauma* **2020**, *8*, tkz002.
(27) Tan, J.; Zhou, J.; Huang, L.; Fu, Q.; Ao, M.; Yuan, L.; Luo, G. Hypertrophic Scar Improvement by Early Intervention With Ablative Fractional Carbon Dioxide Laser Treatment. *Lasers Surg. Med.* **2021**, *53*, 450−457.
(28) Deng, H.; Tan, T.; Luo, G.; Tan, J.; Li-Tsang, C. W. P. Vascularity and Thickness Changes in Immature Hypertrophic Scars Treated With a Pulsed Dye Laser. *Lasers Surg. Med.* **2021**, *53*, 914−921.
(29) Yang, B.; Dong, Y.; Shen, Y.; Hou, A.; Quan, G.; Pan, X.; Wu, C. Bilayer Dissolving Microneedle Array Containing 5-Fluorouracil and Triamcinolone With Biphasic Release Profile for Hypertrophic Scar Therapy. *Bioact. Mater.* **2021**, *6*, 2400−2411.
(30) Chang, H.; Chew, S. W. T.; Zheng, M.; Lio, D. C. S.; Wiraja, C.; Mei, Y.; Ning, X.; Cui, M.; Than, A.; Shi, P.; et al. Cryomicroneedles for Transdermal Cell Delivery. *Nat. Biomed. Eng.* **2021**, *5*, 1008−1018.
(31) Makvandi, P.; Jamaledin, R.; Chen, G.; Baghbantaraghdari, Z.; Zare, E. N.; Di Natale, C.; Onesto, V.; Vecchione, R.; Lee, J.; Tay, F. R.; et al. Stimuli-responsive Transdermal Microneedle Patches. *Mater. Today* **2021**, *47*, 206−222.
(32) Su, Y.; Mainardi, V. L.; Wang, H.; McCarthy, A.; Zhang, Y. S.; Chen, S.; John, J. V.; Wong, S. L.; Hollins, R. R.; Wang, G.; et al. Dissolvable Microneedles Coupled with Nanofiber Dressings Eradicate Biofilms *via* Effectively Delivering a Database-Designed Antimicrobial Peptide. *ACS Nano* **2020**, *14*, 11775−11786.
(33) Yang, J.; Zhang, H.; Hu, T.; Xu, C.; Jiang, L.; Zhang, Y. S.; Xie, M. Recent Advances of Microneedles Used Towards Stimuli-responsive Drug Delivery, Disease Theranostics, and Bioinspired Applications. *Chem. Eng. J.* **2021**, *426*, 130561.
(34) Dixon, R. V.; Skaria, E.; Lau, W. M.; Manning, P.; Birch-Machin, M. A.; Moghimi, S. M.; Ng, K. W. Microneedle-based Devices for Point-of-care Infectious Disease Diagnostics. *Acta Pharm. Sin. B* **2021**, *11*, 2344−2361.
(35) Wang, Z.; Luan, J.; Seth, A.; Liu, L.; You, M.; Gupta, P.; Rathi, P.; Wang, Y.; Cao, S.; Jiang, Q.; et al. Microneedle Patch for The Ultrasensitive Quantification of Protein Biomarkers in Interstitial Fluid. *Nat. Biomed. Eng.* **2021**, *5*, 64−76.

https://doi.org/10.1021/acsnano.1c11016
ACS Nano 2022, 16, 10163−10178

(36) Guo, C.; Li, C.; Vu, H. V.; Hanna, P.; Lechtig, A.; Qiu, Y.; Mu, X.; Ling, S.; Nazarian, A.; Lin, S. J.; et al. Thermoplastic Moulding of Regenerated Silk. *Nat. Mater.* **2020**, *19*, 102−108.
(37) Mu, X.; Yuan, J. S. K., Jr.; Choi, J.; Zhang, Y.; Cebe, P.; Jiang, X.; Zhang, Y. S.; Kaplan, D. L. Conformation-driven Strategy for Rresilient and Functional Protein Materials. *Proc. Natl. Acad. Sci. U. S. A.* **2022**, *119*, DOI: 10.1073/pnas.2115523119.
(38) Zheng, H.; Zuo, B. Functional Silk Fibroin Hydrogels: Preparation, Properties and Applications. *J. Mater. Chem. B* **2021**, *9*, 1238−1258.
(39) Fayzullin, A.; Ignatieva, N.; Zakharkina, O.; Tokarev, M.; Mudryak, D.; Khristidis, Y.; Balyasin, M.; Kurkov, A.; Churbanov, S.; Dyuzheva, T.; et al. Modeling of Old Scars: Histopathological, Biochemical and Thermal Analysis of the Scar Tissue Maturation. *Biology (Basel)* **2021**, *10*, 136−151.
(40) Kloeters, O.; Tandara, A.; Mustoe, T. A. Hypertrophic Scar Model in the Rabbit Ear: a Reproducible Model for Studying Scar Tissue Behavior With New Observations on Silicone Gel Sheeting for Scar Reduction. *Wound Repair Regen.* **2007**, *15*, 40−45.
(41) Chen, L.; Yan, C.; Zheng, Z. Functional Polymer Surfaces for Controlling Cell Behaviors. *Mater. Today* **2018**, *21*, 38−59.
(42) Boopathy, A. V.; Mandal, A.; Kulp, D. W.; Menis, S.; Bennett, N. R.; Watkins, H. C.; Wang, W.; Martin, J. T.; Thai, N. T.; He, Y.; et al. Enhancing Humoral Immunity *via* Sustained-Release Implantable Microneedle Patch Vaccination. *Proc. Natl. Acad. Sci. U. S. A.* **2019**, *116*, 16473−16478.
(43) Tsioris, K.; Raja, W. K.; Pritchard, E. M.; Panilaitis, B.; Kaplan, D. L.; Omenetto, F. G. Fabrication of Silk Microneedles for Controlled-Release Drug Delivery. *Adv. Funct. Mater.* **2012**, *22*, 330−335.
(44) Wen, D.-L.; Sun, D.-H.; Huang, P.; Huang, W.; Su, M.; Wang, Y.; Han, M.-D.; Kim, B.; Brugger, J.; Zhang, H.-X.; Zhang, X.-S.; et al. Recent Progress in Silk Fibroin-based Flexible Electronics. *Microsyst. Nanoeng.* **2021**, *7*, 35−60.
(45) Lammel, A. S.; Hu, X.; Park, S.-H.; Kaplan, D. L.; Scheibel, T. R. controlling silk fibroin particle features for drug delivery. *Biomaterials* **2010**, *31*, 4583−4591.
(46) Lyu, H.; Sun, Z.; Liu, Y.; Yu, X.; Guo, C. Processing-Structure-Properties Relationships of Glycerol-Plasticized Silk Films. *Molecules* **2022**, *27*, 1339.
(47) Deng, J.; Tang, Y.; Zhang, Q.; Wang, C.; Liao, M.; Ji, P.; Song, J.; Luo, G.; Chen, L.; Ran, X.; et al. A Bioinspired Medical Adhesive Derived from Skin Secretion of Andrias davidianus for Wound Healing. *Adv. Funct. Mater.* **2019**, *29*, 1809110−1809123.
(48) Yeo, D. C.; Wiraja, C.; Paller, A. S.; Mirkin, C. A.; Xu, C. Abnormal Scar Identification with Spherical-nucleic-acid Technology. *Nat. Biomed. Eng.* **2018**, *2*, 227−238.
(49) Zhang, J.; Zheng, Y.; Lee, J.; Hua, J.; Li, S.; Panchamukhi, A.; Yue, J.; Gou, X.; Xia, Z.; Zhu, L.; et al. A Pulsatile Release Platform Based on Photo-induced Imine-crosslinking Hydrogel Promotes Scarless Wound Healing. *Nat. Commun.* **2021**, *12*, 1670−1683.
(50) Chan, C. K. F.; Longaker, M. T. Fibroblasts Become Fat to Reduce Scarring. *Science* **2017**, *355*, 693−694.
(51) Corr, D. T.; Gallant-Behm, C. L.; Shrive, N. G.; Hart, D. A. Biomechanical Behavior of Scar Tissue and Uninjured Skin in a Porcine Model. *Wound Repair. Regen.* **2009**, *17*, 250−259.
(52) Wietecha, M. S.; Pensalfini, M.; Cangkrama, M.; Muller, B.; Jin, J.; Brinckmann, J.; Mazza, E.; Werner, S. Activin-mediated Alterations of the Fibroblast Transcriptome and Matrisome Control the Biomechanical Properties of Skin Wounds. *Nat. Commun.* **2020**, *11*, 2604−2624.
(53) Ma, K.; Kwon, S. H.; Padmanabhan, J.; Duscher, D.; Trotsyuk, A. A.; Dong, Y.; Inayathullah, M.; Rajadas, J.; Gurtner, G. C. Controlled Delivery of a Focal Adhesion Kinase Inhibitor Results in Accelerated Wound Closure with Decreased Scar Formation. *J. Invest Dermatol.* **2018**, *138*, 2452−2460.
(54) Joodaki, H.; Panzer, M. B. Skin Mechanical Properties and Modeling: A review. *Proc. Inst. Mech. Eng., Part H* **2018**, *232*, 323−343.
(55) Aarabi, S.; Bhatt, K. A.; Shi, Y.; Paterno, J.; Chang, E. I.; Loh, S. A.; Holmes, J. W.; Longaker, M. T.; Yee, H.; Gurtner, G. C. Mechanical Load Initiates Hypertrophic Scar Formation Through Decreased Cellular Apoptosis. *FASEB J.* **2007**, *21*, 3250−3261.
(56) Weng, W.; He, S.; Song, H.; Li, X.; Cao, L.; Hu, Y.; Cui, J.; Zhou, Q.; Peng, H.; Su, J. Aligned Carbon Nanotubes Reduce Hypertrophic Scar *via* Regulating Cell Behavior. *ACS Nano* **2018**, *12*, 7601−7612.
(57) Gao, Y.; Zhou, J.; Xie, Z.; Wang, J.; Ho, C. K.; Zhang, Y.; Li, Q. Mechanical Strain Promotes Skin Fibrosis Through LRG-1 Induction Mediated by ELK1 and ERK Signalling. *Commun. Biol.* **2019**, *2*, 359−374.
(58) Manzano, S.; Moreno-Loshuertos, R.; Doblare, M.; Ochoa, I.; Hamdy Doweidar, M. Structural Biology Response of a Collagen Hydrogel Synthetic Extracellular Matrix with Embedded Human Fibroblast: Computational and Experimental Analysis. *Med. Biol. Eng. Comput.* **2015**, *53*, 721−735.
(59) Han, Y. L.; Ronceray, P.; Xu, G.; Malandrino, A.; Kamm, R. D.; Lenz, M.; Broedersz, C. P.; Guo, M. Cell Contraction Induces Long-ranged Stress Stiffening in the Extracellular Matrix. *Proc. Natl. Acad. Sci. U. S. A.* **2018**, *115*, 4075−4080.
(60) Hall, M. S.; Alisafaei, F.; Ban, E.; Feng, X.; Hui, C. Y.; Shenoy, V. B.; Wu, M. Fibrous Nonlinear Elasticity Enables Positive Mechanical Feedback Between Cells and ECMs. *Proc. Natl. Acad. Sci. U. S. A.* **2016**, *113*, 14043−14048.
(61) Zhong, Y.; Zhang, J.; Zhang, J.; Hou, Y.; Chen, E.; Huang, D.; Chen, W.; Haag, R. Tumor Microenvironment Activatable Nanoenzymes for Mechanical Remodeling of Extracellular Matrix and Enhanced Tumor Chemotherapy. *Adv. Funct. Mater.* **2021**, *31*, 2007544−2007555.
(62) Li, J.; Jiang, X.; Li, H.; Gelinsky, M.; Gu, Z. Tailoring Materials for Modulation of Macrophage Fate. *Adv. Mater.* **2021**, *33*, 2004172−2004210.
(63) Chu, S. Y.; Chou, C. H.; Huang, H. D.; Yen, M. H.; Hong, H. C.; Chao, P. H.; Wang, Y. H.; Chen, P. Y.; Nian, S. X.; Chen, Y. R.; et al. Mechanical Stretch Induces Hair Regeneration Through the Alternative Activation of Macrophages. *Nat. Commun.* **2019**, *10*, 1524−1535.
(64) Hinz, B. Mechanical Aspects of Lung Fibrosis: a Spotlight on the Myofibroblast. *Proc. Am. Thorac. Soc.* **2012**, *9*, 137−147.
(65) Lin, S.; Quan, G.; Hou, A.; Yang, P.; Peng, T.; Gu, Y.; Qin, W.; Liu, R.; Ma, X.; Pan, X.; et al. Strategy for Hypertrophic Scar Therapy: Improved Delivery of Triamcinolone Acetonide Using Mechanically Robust Tip-concentrated Dissolving Microneedle Array. *J. Controlled Release* **2019**, *306*, 69−82.
(66) Huang, Y.; Peng, T.; Hu, W.; Gao, X.; Chen, Y.; Zhang, Q.; Wu, C.; Pan, X. Fully armed photodynamic therapy with spear and shear for topical deep hypertrophic scar treatment. *J. Controlled Release* **2022**, *343*, 408−419.
(67) O'Reilly, S.; Crofton, E.; Brown, J.; Strong, J.; Ziviani, J. Use of Tape for the Management of Hypertrophic Scar Development: A comprehensive review. *Scars Burn Heal* **2021**, *7*, 1−17.
(68) Huang, D.; Zhao, D.; Wang, X.; Li, C.; Yang, T.; Du, L.; Wei, Z.; Cheng, Q.; Cao, H.; Liang, Z.; et al. Efficient delivery of Nucleic Acid Molecules into Skin by Combined Uuse of mMicroneedle Roller and Flexible Interdigitated Electroporation Array. *Theranostics* **2018**, *8*, 2361−2376.
(69) Corr, D. T.; Hart, D. A. Biomechanics of Scar Tissue and Uninjured Skin. *Adv. Wound Care (New Rochelle)* **2013**, *2*, 37−43.
(70) Cheng, L.; Sun, X.; Zhao, X.; Wang, L.; Yu, J.; Pan, G.; Li, B.; Yang, H.; Zhang, Y.; Cui, W. Surface Biofunctional Drug-loaded Electrospun Fibrous Scaffolds for Comprehensive Repairing Hypertrophic Scars. *Biomaterials* **2016**, *83*, 169−181.

https://doi.org/10.1021/acsnano.1c11016
ACS Nano 2022, 16, 10163−10178